Politecnico di Torino

Politecnico di Torino

Master's Degree Course in Biomedical Engineering

A.a. 2020/2021

Sessione di Laurea Luglio 2021

Linking Eulerian-based wall shear stress topological skeleton to near-wall low-density lipoproteins and oxygen transport in arterial flow

Supervisors

Prof. Umberto Morbiducci

Prof. Diego Gallo

Ing. Giuseppe De Nisco

Ing. Karol Calò

Candidate:

Lucia Chiarolanza

Alla mia famiglia,
per avermi sempre sostenuta.

"Be happy for this moment. This moment is your life."
– Omar Khayyam

Contents

Abstract

Atherosclerosis is a systemic inflammatory disease of the large and medium-sized arteries that involves a characteristic accumulation of fatty material (e.g. lipid, cholesterol) on the inner surface of the vessel walls. This process leads to the formation of atherosclerotic plaques which in turn cause the hardening, thickening and loss of elasticity of the arterial wall.

Mass transport in arteries plays a key role in vascular disease. In particular high levels of low-density lipoproteins (LDL) and low levels of oxygen in the arterial wall are involved in the atherosclerotic process. In addition to that, also hemodynamic factors, in particular wall shear stress (WSS), contribute to the onset and progression of atherosclerosis. For this reason, in the last decades, several descriptors have been proposed as hemodynamic markers of "disturbed flow" and personalized computational fluid dynamics (CFD) has been adopted to elucidate the links (if any) among disturbed flow, atherogenesis and mass transport in human arteries. In this context, a growing interest has recently emerged on WSS vector field topological skeleton, due to its ability to properly describe near-wall mass transfer, overcoming the main limitation represented by the high computational costs necessary to model mass transfer solving the conventional advection-diffusion equations.

The present thesis aims to test the ability of a recently-proposed Eulerian-based method for the identification of WSS topological skeleton, to provide a reliable template of the near-wall mass transport in subject-specific computational hemodynamic models of human arteries.

More in detail, in this study blood flow, together with LDL and oxygen mass transfer, was simulated using image-based CFD models of carotid bifurcation, right coronary artery (RCA) and left coronary artery (LAD).

The relationship between the well-established WSS-based hemodynamic descriptors, WSS topological skeleton and the LDL/oxygen polarization at the vessel wall has been investigated through a co-localization analysis. The results confirm the ability of the Eulerian-based method for the identification of WSS topological skeleton to

provide an effective template of the mass transport in arteries with a significative reduction of both the computational costs and the complexity of classical techniques.

Chapter 1

1 Introduction

1.1 The cardiovascular system

The cardiovascular system includes three interrelated components: the blood, the heart and the blood vessels. Its main function is providing nutrients and oxygen to the body tissues while removing wastes produced by metabolism [1].

Two closed circuits compose the cardiovascular system: the pulmonary circulation – which carries blood to and from the lungs for the uptake of oxygen and the removal of carbon dioxide – and the systemic circulation – carrying oxygenated blood throughout the body and picking up carbon dioxide from body tissues.

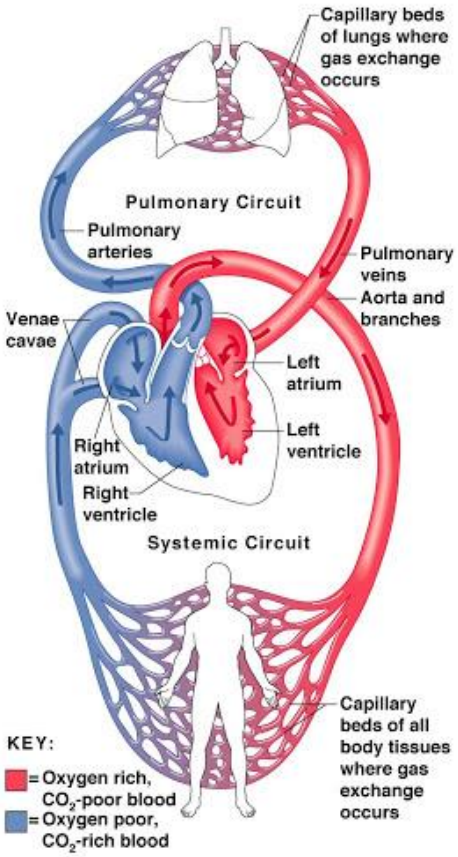

Figure 1.1 Pulmonary and systemic circulation.

The two circuits are placed in series as meaning that the output of one is the input of the other (**Fig. 1.1**) [1, 2].

The systemic circulation starts from the left ventricle, ejecting bright red, oxygen-rich blood into the aorta. From the aorta, the blood divides into separate streams, entering progressively smaller systemic arteries that carry it to all body's tissues - except for the air sacs of the lungs, which are supplied by pulmonary circulation. Then, the blood moves from the arteries to the smaller diameter arterioles, up to the systemic capillaries, where the exchange of nutrients and gases occurs across the thin capillary walls. Blood unloads oxygen and gains carbon dioxide. Deoxygenated blood enters the systemic venules, which merge to form larger systemic veins. This complex system of veins drains into the superior vena cava, inferior vena cava, or coronary sinus, which in turn empty into the right atrium [1, 2].

The pulmonary circulation carries the dark red, oxygen-poor blood from the right ventricle into the pulmonary trunk, which branches into pulmonary arteries that carry blood to the lungs. Between the pulmonary capillaries and the alveoli, the exchange of oxygen and carbon dioxide that the body has produced occurs. The newly oxygenated blood then flows into pulmonary veins and returns to the left atrium of the heart [2].

The three major types of blood vessels are arteries veins and capillaries. Arteries can in turn be divided into the largest or elastic arteries, the medium-sized or muscular arteries and the smallest arteries called arterioles. The smallest veins are called venules whilst capillaries are the smallest blood vessels [2].

The walls of arteries and veins are structured in three distinct layers: the tunica intima, media and adventitia (or externa).

The innermost layer is the tunica intima, which is in direct contact with the blood as it flows in the lumen. This tunic contains a single layer of endothelial cells – the endothelium – and a small amount of loose connective tissue – the subendothelial layer (basement membrane). Separating the tunica intima from the media is a thin and fenestrated layer of elastic fibers called the internal elastic lamina [1].

The tunica media comprises a multilayer of smooth muscle cells, elastic fibers and connective tissue. In physiological conditions, muscle cells regulate the vessel's diameter: decrease and increase in it are known as vasoconstriction and vasodilatation, respectively. The tunica media is thicker in arteries than in veins, because the arteries, especially the

larger ones, need a greater quantity of elastic fibers to accommodate the pressure variations of blood stream. The boundary between the tunica media and adventitia is another elastic layer of fibers: the external elastic lamina. As the internal one, it also has several window-like openings [1].

The outermost layer of a vessel wall, the tunica adventitia, is a network of elastic and collagen fibers. The larger arteries and veins also have tiny blood vessels in their tunica externa called vasa vasorum. Their function is to supply the tissue, by contrast, the smaller vessels get nutrients by luminal blood [2].

The summary of these tunics covers features that are in common to arteries as well as veins. However, modifications in this basic structure occurs and they are correlated to the functional variations [1].

This is exactly why the capillaries have a very different wall structure than the arteries and veins. They lack both a tunica media and adventitia. Thanks to the only single layer of endothelial and subendothelial cells, they make possible the exchange of gases and nourishment between blood and all body parts.

1.1.1 The heart

The heart is a hollow muscular organ on which all the functions of the cardiovascular system depend. It can be thought of as two pumps: the right side receives deoxygenated blood from the tissues and pumps it into the lungs in order to pick up oxygen and remove carbon dioxide, while the left side receives the oxygen-rich blood from the pulmonary system and pumps it to all body tissues in order to provide nourishment [2].

The human heart is located into the thoracic cavity, in the space between the left and right lungs (mediastinum). It assumes an oblique position in the thorax, with about two-thirds of its mass to the left of midline. It rests on the diaphragm, anteriorly it is protected by the sternum and costal cartilages and posteriorly it lies on the column, at the thoracic vertebrae [4].

A roughly conical shape characterizes the human heart with the major base that looks up, back and to the right and the apex which points down, forward and left [4].

In adults, the average weight of the heart is 300 grams but there are individuals and sex variations. It is normally slightly larger than a closed fist, being approximately 12 cm long, 9 cm wide and 6 cm thick [1].

The heart is surrounded by a membrane called the pericardium. It comprises two continuous sacs: the superficial fibrous pericardium and the inner serous pericardium. These two sacs have different structures and functions [3].

The fibrous pericardium is composed of tough, inelastic, dense and irregular connective tissue and its function is to prevent the overstretching of the muscle, provide protection and anchor it in the mediastinum. The serous pericardium is a thin and delicate membrane forming a double layer around the heart: the outer parietal pericardium, fused with the fibrous pericardium and the innermost visceral layer (epicardium), which adheres to the heart muscle. Between the two layers of the serous pericardium is the pericardial cavity containing a thin film of lubricating fluid known as the pericardial fluid which reduces friction between the membranes during the heart contraction [3].

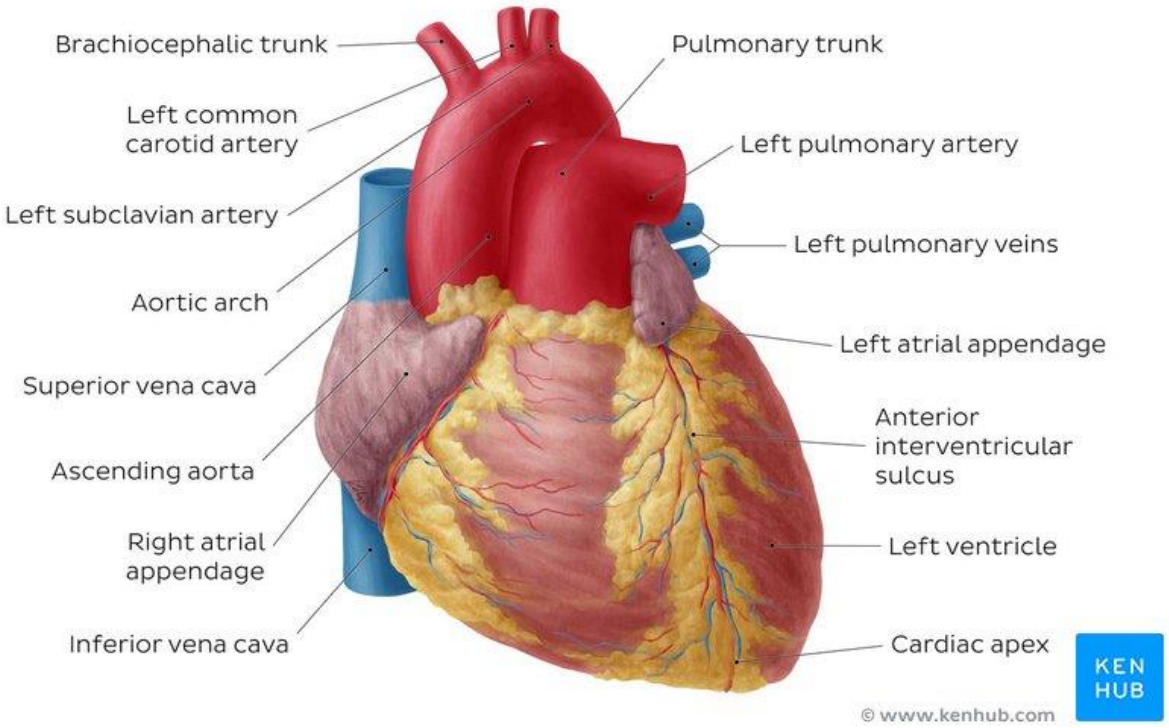

Figure 1.2 Anterior view of the heart.

The heart wall is made up of three layers: from the inside out there are the epicardium, the myocardium and the endocardium.

The superficial epicardium is a thin membrane covering the heart and large vessels; the middle myocardium is a thick layer of muscle tissue while the deeper endocardium is made up endothelial cells and covers the cardiac valves [1].

The heart is divided into four chambers: the two upper receiving chambers are the right and left atrium whilst the lower pumping ones are the right and left ventricles (**Fig. 1.2**). As mentioned before, the right atrium and ventricle form the right heart, which receives and pumps oxygen-poor blood; the left atrium and ventricle form the left heart, which receives and pumps oxygenated blood [3].

The right atrium receives blood from three veins: the superior vena cava – draining blood from the upper parts of the body – the inferior vena cava – which drains blood from the lower parts – and, lastly, the coronary sinus. The left atrium receives blood from four pulmonary veins returning to the lungs. On the anterior surface of the atria is a wrinkled saccular structure called the auricle: its function is to increase the internal capacity of the atrium, allowing it to accommodate a greater volume of blood. Between the two atria is a tiny dividing wall, the interatrial septum [1].

The right ventricle receives blood from the right atrium and pumps it into the lungs (pulmonary system). The left ventricle receives blood from the left atrium and pumps it through the body via aorta. The two ventricles are separated by another lining called the interventricular septum [2].

The chambers carry out their work thanks to four cardiac valves. Between the atria and ventricles are two atrioventricular valves: the tricuspid valve – which lies between the right atrium and the right ventricle – and the bicuspid (mitral) valve – which lies between the left atrium and the left ventricle. Two other valves are situated at the outlet of each ventricle: the pulmonary valve, that is located between the right ventricle and the pulmonary arteries, and the aortic valve that lies between the left ventricle and the aorta. The purpose of each of the four valves is to allow the one-way flow of the blood, preventing its backflow by opening and closing where appropriate [3].

The heart performs its function through alternate phases of contraction and relaxation, that give rise to the so-called cardiac cycle. The contraction phase is called systole, the relaxation phase is called diastole. A single entire cardiac cycle comprises all

the events associated with one heartbeat and lasts about 0.8 seconds. The heart rate is 75 beats per minute [1].

The stimulus for contraction is provided by some cardiac muscle fibers capable of spontaneously and rhythmically generating action potentials, performing two important functions: they act as a pacemaker by regulating the rhythm of the heart and form the conduction system allowing the heart cavities to contract coordinately [2].

1.1.2 The carotid arteries

The left and right carotid arteries are two large arterial trunks located on the sides of the neck. Together with the vertebral arteries, they supply rich-oxygen blood to the head and neck [5].

Anatomically, each carotid can be divided in three parts: common carotid artery (CCA), external carotid artery (ECA) and internal carotid artery (ICA). The common carotid arteries differ in their origin: the right CCA arises from the brachiocephalic trunk (also called innominate artery), while the left CCA originates directly from the aortic arch. Each common carotid artery runs through the neck up to the upper border of the thyroid cartilage, where they divide into the external and internal carotid arteries [6].

The ICA ascends through the carotid canal in the temporal bone into the cranial cavity, suppling blood to the brain. Then it divides into the ophthalmic branch, which supply the eye and its appendices, and the anterior and middle cerebral arteries. This vessel is distinguished by having curvatures and twists along its course [5].

The ECA supplies oxygen-rich blood to the face, scalp, and neck. It ascends through the upper part of the side of the neck and behind the lower jaw into the parotid gland, rapidly decreasing in size. It gives off eight branches which can be grouped in four sets: anterior, posterior, ascending and terminal.

In the child, the ECA can be smaller than the ICA, while in the adult the two vessels have the same size [6]. Due to its anatomical features, the carotid artery is a preferred site of atherosclerotic plaque development. The plaques form especially at the carotid sinus (or carotid bulb), that is an ICA dilatation situated close to the bifurcation that divides the common carotid into internal and external carotid artery. The plaques, narrowing the vessel, decrease the blood supply to the brain, increasing the risk of stroke or brain attack (**Fig. 1.3**) [8].

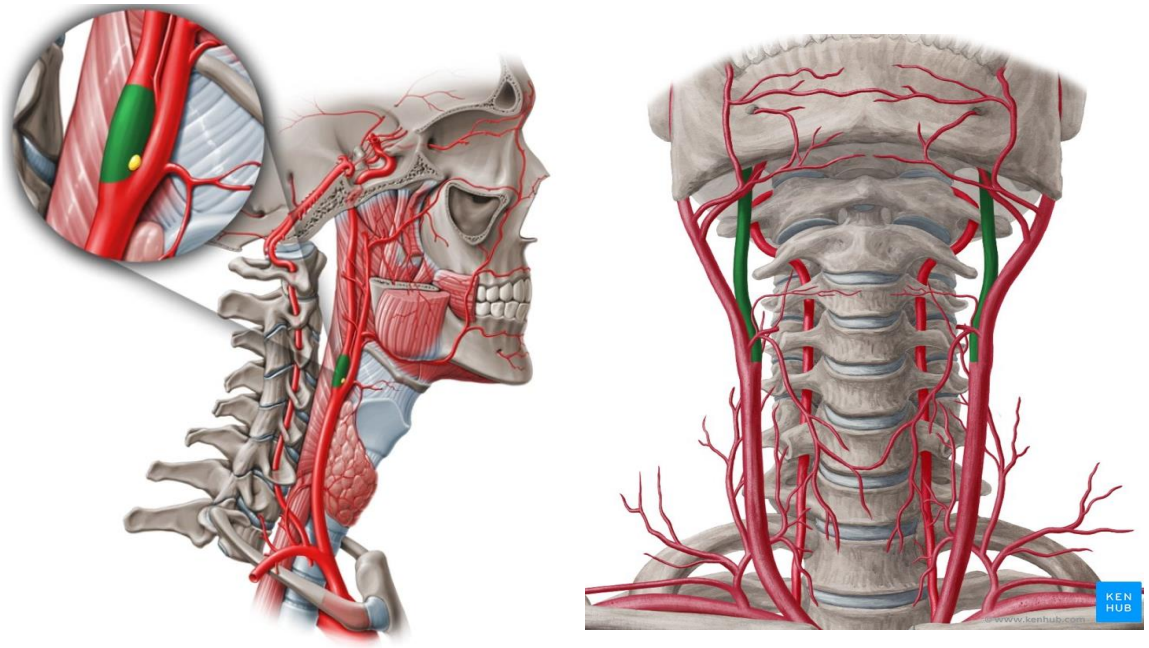

Figure 1.3 Carotid arteries: the left side shows the lateral view with a focus of the carotid sinus (green) and the carotid body (yellow) while on the right there is a frontal view.

1.1.3 The coronary arteries

The myocardium has its own network of blood vessels, the coronary circulation, to meet its vital needs. It is supplied with blood by the right and left coronary arteries. These vessels branch from the ascending aorta, at the location of the aortic (semilunar) valve and encircle the heart within the atrioventricular sulcus, the depression between the atria and ventricles [2].

Two branches arise from both the right and left coronary arteries to serve the atria and ventricles.

The left coronary artery (LCA) divides into the anterior interventricular branch, or left anterior descending (LAD) artery, and the circumflex branch. The former courses within the anterior interventricular sulcus to serve both ventricles, while the circumflex branch lies in the coronary sulcus and supplies oxygenated blood to the walls of the left atrium and left ventricle [1, 2].

The right coronary artery (RCA) continues inferior to the right auricle and ultimately divides into the posterior interventricular and marginal branches. The posterior interventricular branch courses through the posterior interventricular sulcus to provide nourishment to the wall of the two ventricles, whilst the right marginal artery, in the

coronary sulcus, supplies the walls of the right ventricle (**Fig. 1.4**). The main trunks of the right and left coronaries connect each other on the posterior surface of the heart. These connections, called anastomoses, provide detours for the blood if a main branch is partially blocked [2].

One of the most common cardiovascular disease is the coronary artery disease (CAD). It involves the hardening of the artery walls and the reduction of blood flow to the heart muscle due to the accumulation of atherosclerotic plaques in coronary arteries. The onset and development of atherosclerosis will be discussed in the next section [1].

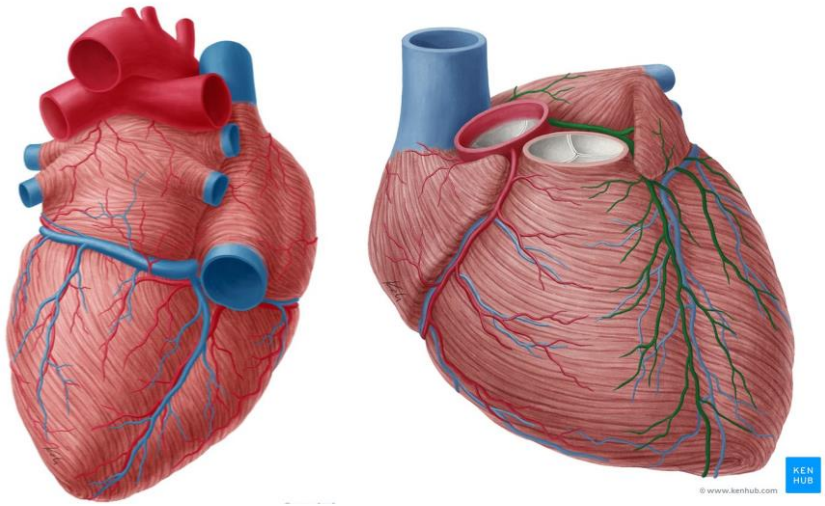

Figure 1.4 Two different views of the heart with the detail of the coronary arteries (blue vessels).

1.2 Atherosclerosis

Atherosclerosis is the most common form of arteriosclerosis, a term which refers to a group of diseases characterized by loss of elasticity and thickening of the walls of arteries. In detail, atherosclerosis is a progressive disease characterized by the formation in the walls of large and medium-sized arteries of lesions called atherosclerotic plaques, made up of lipids, inflammatory cells and connective fibrous tissue. The arteries most affected by this pathology are the coronary arteries, the carotid arteries and the aorta [1, 9].

1.2.1 Risk factors

Atherosclerosis is characterized by a multifactorial etiology. Although the exact cause is unknown, the disease may start with an injury to the inner layer of an artery.

The main risk factor is the high serum cholesterol concentration, directly linked to lifestyle and unhealthy diet. This is associated with other factors, such as obesity, lack of exercise, smoking and stress which predispose to the development of atherosclerotic plaques.

There are also some pathological situations that favor the onset of the disease, such as hypertension, hypothyroidism and diabetes mellitus.

Atherosclerosis can also depend on uncontrollable factors that include age, genetics and sex. In fact, the prevalence of atherosclerosis increases with age and men develop atherosclerosis more often than women.

In addition to the previous factors, there is also evidences linking the development of atherosclerotic plaques to impaired local hemodynamics, as occurs in the presence of bifurcations, branches or accentuated curves [10].

1.2.2 Pathogenesis

Atherosclerosis is a slow and progressive disease that may begin as early as childhood. This condition is a process in which deposits of fatty material (plaque) form inside the arterial walls, reducing or completely blocking blood flow.

Although the exact causes are unknow, studies suggest that atherosclerosis starts with damage to the inner layer of an artery (called endothelium) [11].

Substances that travel in the blood, such as cholesterol, fats and cell waste products, accumulate in the damaged area of the arterial wall. The chemical reactions that occur in this site cause oxidation of the cholesterol molecules. This initiates an inflammatory process in which endothelial cells on the damaged site release chemicals. In response, monocytes in the blood flow travel to the damaged site. The stimulation of oxidized cholesterol converts monocytes into macrophages, which start to ingest cholesterol molecules. After that, the macrophages turn into foam cells and accumulate to form plaque. As the plaque increases in volume, the arterial wall thickens and hardens.

At the same time, the smooth muscle cells in the arterial wall begin to multiply. Most of them migrate to the surface of the plaque. These cells contribute to the formation of a fibrous cap that covers the plaque [12].

As a result, the passage through the artery narrows reducing the blood flow and the amount of oxygen received by the organs. Over time, the cap may erode and open, releasing the plaque in the bloodstream. Plaque flows downstream creating a blood clot that can stop blood flow [12].

1.2.3 Consequences of atherosclerosis

Atherosclerosis-related diseases are currently the major cause of death in many industrialized countries. Although atherosclerosis is often considered a heart problem, it can affect any artery in the human body. As a result, different diseases may develop based on which arteries are affected [11].

The major complications of atherosclerosis are associated with occlusion or inadequate blood flow to organs perfused by the affected artery.

When atherosclerosis narrows the arteries close to the heart, coronary arteries disease (CAD) may develop, which can cause chest pain (angina pectoris), a heart attack or heart failure. Atheromas can also narrow the arteries close to the brain, developing carotid artery disease, which can cause an ischemic attack or stroke. When atherosclerosis narrows the peripheral arteries, peripheral artery disease can develop, which leads to circulation problems in arms or legs. This causes a loss of sensitivity in the limbs and, in rare cases, it can cause tissue death. Atherosclerosis can cause the arteries leading to the

kidneys to narrow, affecting the kidney function. Lastly, atherosclerosis can also cause aneurysms, that is a bulge in the wall which can occur anywhere in the body [11].

However, changes in the mechanical properties of the arteries may lead to many non-occlusive complications. The aorta sometimes becomes mechanically unstable and dilate, forming aneurysms. Over time, the aorta loses its elasticity and may calcify. Blood ejected into a rigid aorta encounters increased flow resistance that causes an increased cardiac work. Also these factors may trigger the heart failure and stroke [11].

1.3 Low-density lipoproteins

Lipoproteins, as the name suggests, are high macromolecular weight aggregates of proteins and lipids that circulate in the blood plasma. Such complexes are important to collect and transport lipids to the body cells for their growth requirement and energy storage [14].

Lipoproteins have a micellar structure. The inner layer (core) is composed of the transported lipids (cholesteryl esters and triglycerides), while the outer layer is composed of a single layer of unesterified cholesterol, phospholipids and specific proteins, known as apo-lipoproteins (**Fig. 1.5**). These proteins contain amphipathic regions which enable them to bind lipids and at the same time be transported in the blood vessels [13].

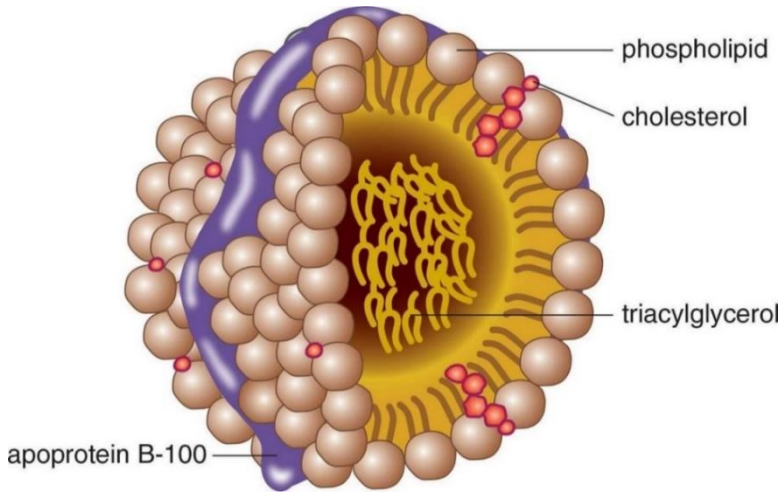

Figure 1.5 Structure of a lipoprotein.

There are many different types of lipoproteins with the same general structure, but with very different ratios between lipid and protein content, as well as different protein types. This study focuses on low-density lipoproteins (LDL) because their metabolism is closely interrelated with the onset and progression of atherosclerosis [14].

Low-density lipoproteins originate from the catabolism of chylomicrons and very low-density lipoproteins and transport most lipids deposited in the atherosclerotic lesions. Their protein component is mainly composed of ApoB-100, but also other proteins such as ApoE and ApoC-III which modulate its atherogenicity despite their low concentration [13, 15, 16].

ApoB-100 is a large protein of 515 KDa with different functional domains such as an LDL-receptor binding site, lysine and arginin-rich segments and many binding sites for glycosaminoglycans that promote their accumulation in the arterial wall. The entry and retention of LDL in the subendothelial layer mainly depend on its high plasma levels, but also on other features as lipoprotein size, amount of cholesterol and endothelial permeability [24, 25].

Once in the arterial intima, the extracellular matrix (ECM) promotes lipoprotein binding. The major components of ECM are collagen, elastin and proteoglycans, which are considered as the most-important lipoprotein-retaining molecules in the subendothelial layer. Here, LDL undergo several modifications, displaying different features from those of native LDL that make them even more atherogenic [14, 17].

1.3.1 LDL modifications

As stated before, in the arterial wall LDL particles change their general structure because of the action of several oxidants (lipoxygenase, myeloperoxidase, free radicals, etc.), proteolytic and lipolytic enzymes (kinase, tryptase, sphingomyelinase etc.) and hydrolytic enzymes (esterase). Aggregation and oxidation are the two main modifications of LDL particles [17].

Aggregated LDL

Modifications of the surface structure of LDL lead to self-aggregation of LDL particles that can result in loss of particle stability. This affects interactions between particles and causes their aggregation. This brings the surfaces of different LDL particles into contact, but does not unite the particles so, does not change the size of individual particles. If modifications are sufficiently extensive, energetic stabilization will result in a subsequent fusion of the attached particles, increasing their atherogenicity. It is important to note that particle aggregation is, in general, a reversible reaction, whereas particle fusion is an irreversible phenomenon (**Fig. 1.6**) [18]. Aggregated LDL (agLDL) bring to a massive intracellular cholesteryl ester accumulation in the vascular smooth muscle cells and in macrophages leading to foam cell formation, the main feature of early atherosclerotic lesion. In vitro studies have shown that native LDL (unmodified LDL) are taken up very slowly by macrophages and vascular smooth muscle cells. However, after

aggregation modifications, agLDL are rapidly absorbed by the macrophages and vascular smooth muscle cells [21, 22, 23].

It is still unclear the mechanism involved in agLDL uptake by macrophages. While some authors suggest a phagocytic process, others have defined a new internalization mechanism called pathocytosis, which consists of capturing several agLDL particles by means of vesicular membrane formations. Moreover, recent studies have demonstrated that agLDL can be internalized by macrophages through LDL receptor-related protein 1 (LRP-1) [14].

Oxidated LDL

In contrast to the other LDL modifications, oxidatively modifications change both the protein and lipid components. This modification is caused by the activity of different enzymes in the arterial intima (15-lipoxigenase, myeloperoxidase, heme-oxydase, etc.) but also by the presence of NO synthase and NADPH oxidase that generate free radicals capable of oxidizing LDL [18].

According to several studies, oxidized low-density lipoprotein (oxLDL) play a key role in the development of atherosclerotic lesions. This cause endothelial injury, including activation, dysfunction, necrosis, and apoptosis of the cells [19].

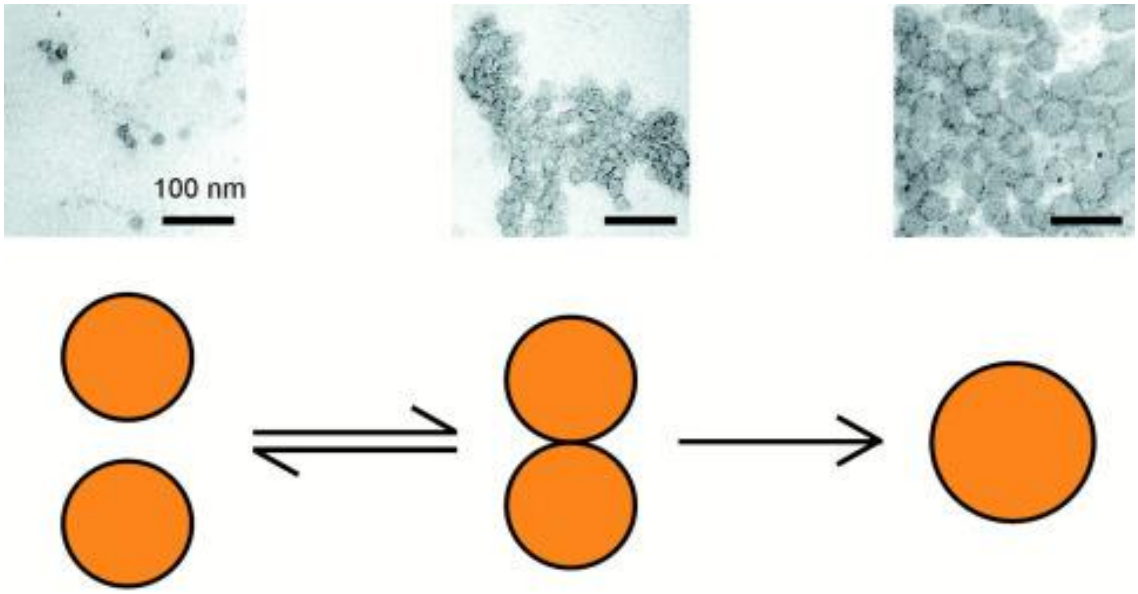

Figure 1.6 Aggregation and fusion of LDL: native LDL (left), aggregated LDL (middle) and fused LDL (right).

A specific family of receptors present in the vascular smooth muscle cells, monocytes and macrophages are responsible for the oxidated lipoproteins uptake by the endothelial cells. They are the scavenger receptors, such as type 1 scavenger receptor (SR-A1) and type 2 (SR-A2) [20].

1.4 Oxygen transport

Oxygen is transported in the blood through two distinct mechanisms: its dissolution in the plasma and its binding to hemoglobin. Oxygen, however, is poorly soluble in plasma (less than 2 percent of the total amount), and it is not enough to satisfy the metabolic demands of the tissues. A specific carrier is required: hemoglobin (Hb). It is a globular protein contained in red blood cells (also called erythrocytes), responsible for transporting most of oxygen in the blood stream. This protein is made up of 4 subunits. Inside each one there is the heme group, with a metal core represented by an iron atom (**Fig. 1.7**). Each iron atom can reversibly bind and then release an oxygen molecule. Thus, each Hb molecule can bind four oxygen molecules. But there are other determinants, such as the partial pressure of oxygen, that is its concentration in the blood, and the affinity of Hb itself to oxygen [26].

In the arterial wall there are two principal pathways for oxygen transport. The outer layers (adventitia and the outer media) receive oxygen from the vasa vasorum, a network of micro-vessels. While the innermost layers (intima and the inner media) pick up the oxygen directly from the blood stream.

Recent studies demonstrated that the penetration of the vasa vasorum network across the wall depends on the arterial thickness. In fact, in the healthy arteries, vasa vasorum enter the adventitia activating a normal blood flow to the wall of this arteries. Instead, in the atherosclerotic vessels, vasa vasorum proliferate also into the intima in order to provide nourishment to the thickened vessel. Therefore, such vasa vasorum have a very thin wall which can rupture very easily, contributing to plaque disruption and thrombosis [29, 30].

In vivo studies demonstrated the presence of a trans-arterial oxygen gradient in normal aortas. From the lumen to the intima oxygen tension drops precipitously: this suggests a large oxygen transport resistance in this region of the wall. Then, from the intima to the media, oxygen tension drops more gradually satisfying the oxygen demand

of the smooth muscle cells in the media. Lastly, the oxygen tension continues to drop gradually in the outer layers as fibroblasts and smooth muscle cells consume oxygen [28].

1.4.1 The role of oxygen transport in atherosclerosis

Atherosclerosis is often related with a small amount of oxygen within the layers of the arterial walls. According to the hypoxia theory of atherosclerosis, a high ratio of oxygen requirement and its supply in the arterial wall play a key role in the development of the vascular disease. In fact, it was observed a colocalization of atherosclerotic plaques

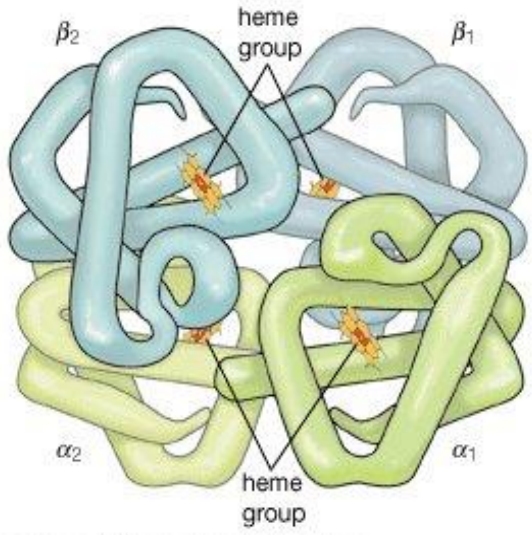

Figure 1.7 Structure of hemoglobin.

and regions in which significant hypoxia exists. This hypoxic condition may change the metabolism and function of many cell types in the arterial wall [31].

The biomolecular pathways in normoxic and hypoxic conditions were analyzed and compared. The transcription factor known as HIF-1α (hypoxia-inducible factor-1α) is the main regulator of the hypoxic response in the cells. Under normoxic conditions, which means physiological levels of oxygen greater than 40 mmHg, HIF-1α becomes targeted for degradation by HIF prolyl-hydroxylase (PHD). The resulting conformational change promotes its binding to VHL complex which in turn targets HIF-1α for ubiquitination and rapid proteasomal degradation. In hypoxic conditions, instead, HIF-1α gradually accumulates in the cells because its degradation is inhibited. This leads to its nuclear translocation and HIF-1α target gene expression. HIF-1α target genes mediate

changes in the function and metabolism of the cells such as glycolysis, angiogenesis, proliferation, and inflammation [32].

This HIF-1α activation by hypoxia is the canonical pathway, but recent studies discovered that HIF-1α can be activated non-canonically through a different mechanism. These studies explained that HIF-1α can be activated by disturbed blood flow (which means a low and oscillating shear stress on the surface of endothelial cells) leading to high levels of HIF-1α. This over-expression of HIF-1α lead to a dysfunction of endothelial cells and subsequent atherogenesis (**Fig. 1.8**) [38, 39].

Thus, hypoxia inducted by disturbed flow, and disturbed blood flow itself in vascular bifurcations and branching leads to a lower oxygen transport across the layers of the artery wall, promoting the development of atherosclerosis Moreover, many cardiovascular risk factors are associated with vasa vasorum compression reducing their perfusion and oxygenation.

As a consequence, their dysfunctional neovascularization, in response to hypoxia, also contributes to plaques inflammation [32].

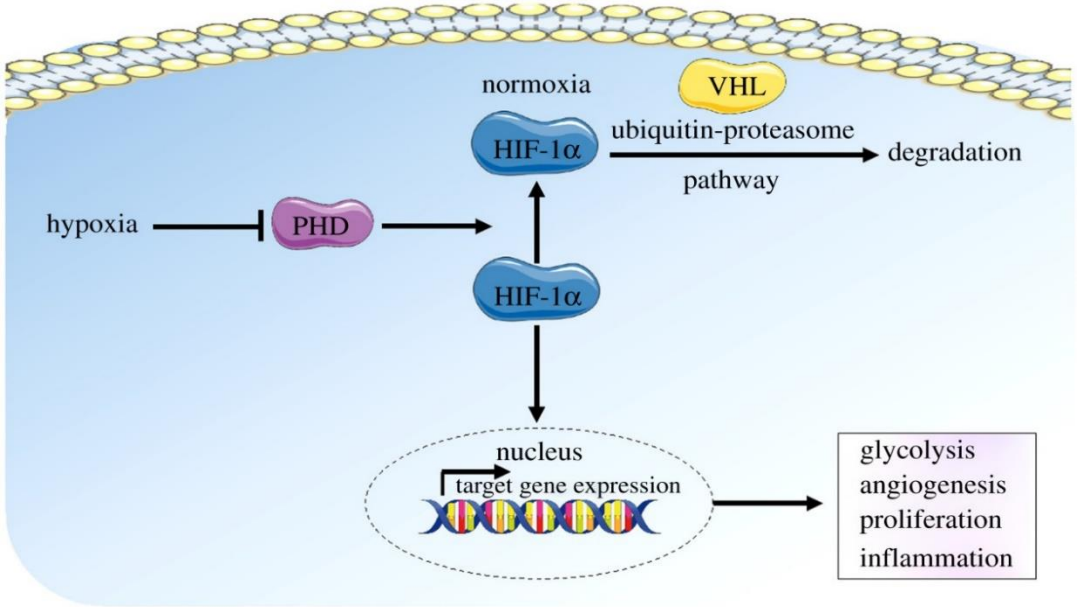

Figure 1.8 Schematic of normoxing and hypoxic signaling.

1.5 The role of hemodynamics in atherosclerosis

Atherosclerosis is a complex and multifactorial disease, influenced by local biological, hemodynamic and systemic factors.

As for hemodynamics, there is much evidence suggesting that the onset and development of atherosclerotic plaques occur in regions characterized by the so-called *aggravating flow events* (or "disturbed flow") such as flow separation and reattachment, vortical flows and stagnation point flows. These fluid dynamics patterns are strictly related to the so-called *abnormal biological events* (e.g. endothelial cell dysfunction, enhanced wall permeability, wall influx of LDL and monocytes) which in turn promote the progression of the vascular disease.

Among hemodynamics forces, wall shear stress (WSS) plays an essential role in preserving normal physiological conditions. Arteries can change their conformation in order to adapt to long term variations of these forces: they dilate their diameter in presence of increased WSS and remodel to a small diameter if subjected to decreased WSS values [33].

Several studies have proposed low and oscillatory WSS values as a marker of disturbed hemodynamics. Endothelial cells are sensitive to changes in modulus and direction of WSS: as shown in **Fig. 1.9**, in presence of laminar and unidirectional flow, cells tend to organize along the principal direction of motion; on the contrary, cells subjected to low and multidirectional flows assume a polygonal conformation with a lack of intercellular junctions, increasing the permeability of the atherogenic molecules.

In order to quantify the role of hemodynamics on the onset of the vessel disease, several descriptors have been proposed over the years. Concerning the near-wall hemodynamics, three WSS-based descriptors have been introduced: the time average wall shear stress (TAWSS), the oscillatory shear index (OSI) and the relative residence time (RRT). These descriptors are able to localize the areas at the vessel wall characterized by low/oscillatory WSS values, as detailed in the next chapter.

Nevertheless, recent evidences have underlined how currently considered WSS-based descriptors may oversimplify the complex hemodynamics features to which the luminal surface is subjected. The exposure to low and oscillatory WSS is, in fact, a significant but moderately weak predictor of lesions localization and development or endothelial dysfunction at the early stage of the disease [35, 56].

In this context, a more in-depth analysis is needed to identify more effective WSS-based hemodynamic indicators.

In these circumstances the topological skeleton of the WSS vector field, based upon dynamical system theory is receiving increasing interest [35, 56]. WSS topological skeleton is composed of fixed points, where WSS locally vanishes, and stable/unstable manifolds identifying expansion/contraction regions connecting fixed points.

Recent studies have demonstrated that the WSS topological skeleton regulates the near-wall biochemical transport in arteries, which plays an important role in the vascular pathophysiology (e.g. atherosclerosis) [56].

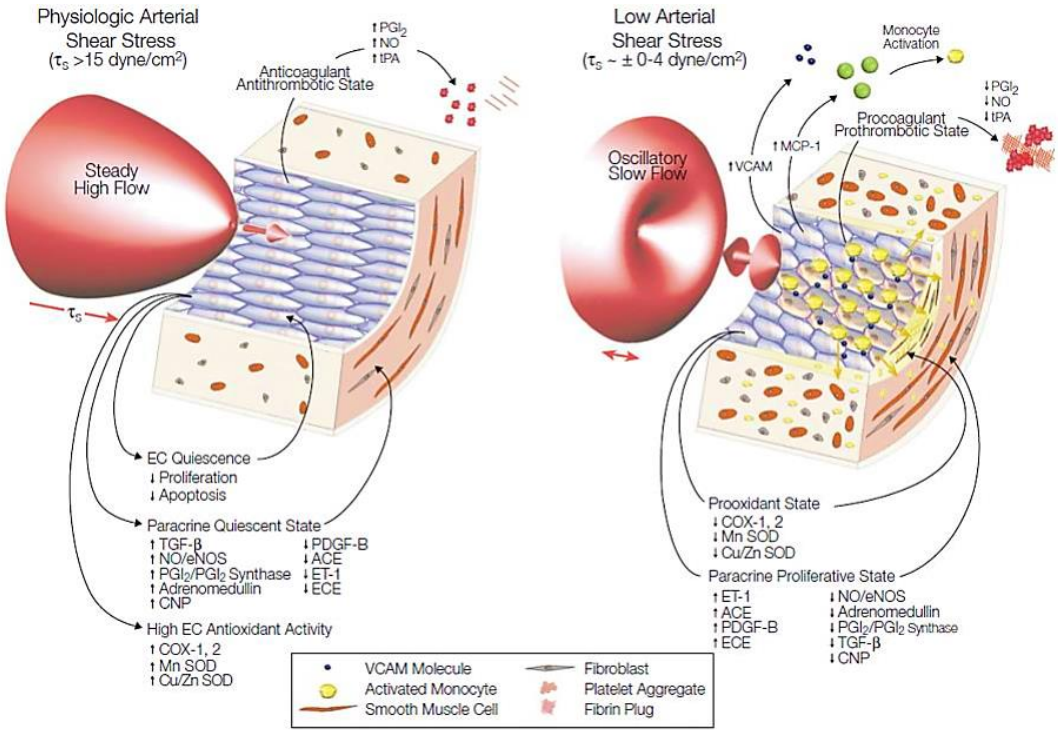

Figure 1.9 Modifications of the endothelial cells in response of laminar unidirectional flow (left) and oscillatory slow flow (right).

1.6 Aim of the study

Mass transport plays an essential role in vascular pathophysiology [34]. In this regard, several studies have been conducted on the mechanisms of mass trasport of the species involved in the vessel wall disease, such as LDL and oxygen molecules. In order to analyze the role of hemodynamic forces on the endothelial lining, several descriptors have been proposed over the years.

As previous stated, the well-established WSS-based descriptors, characterizing the low/oscillatory WSS phenotype, tend to oversimplify the complex milieu to which

the luminal surface is exposed. For this reason, the interest of the scientific community has shifted towards the analysis of the WSS topological skeleton, characterized by WSS fixed points (where the WSS vector field vanishes) and manifolds (i.e., WSS expansion/contraction regions linking fixed points) [35].

The role of WSS topological skeleton in cardiovascular disease is still poorly investigated. However, recent works have been demonstrated how some WSS topological skeleton features may be a clear indicator of wall degradation in ascending thoracic aorta aneurism [36] and long-term restenosis after carotid endarterectomy [37].

The biological relevance of WSS topological skeleton lies in the ability to quantitatively assess the complex and highly dynamic features of the WSS vector field and the strong relation with disturbed flow features such as stagnation, separation and recirculation.

Very recently, a Eulerian-based method for the characterization of WSS topological skeleton was proposed [56]. Such method uses the divergence of the normalized WSS vector field to approximate WSS manifolds, with reduced computational costs and methodological complexity compared to the classical Lagrangian techniques [35].

The aim of this work is to test the ability of the recently-proposed Eulerian-based method to provide a template of blood-to-wall mass transfer in patient-specific computational hemodynamics models of human arteries. To do so, the performance of this new method has been compared with the classical WSS-based descriptors of disturbed flows.

Chapter 2

2 Materials and methods

In this thesis, the study of arterial blood flow and LDL and oxygen transport in blood was conducted using image-based computational fluid dynamics (CFD). Such an approach consists in the integration of clinical imaging inside an *in-silico* framework [40].

Typically, all CFD algorithms cover three main steps called *pre-processing*, *solving* (or simulation) and *post-processing*. In the pre-processing, the model geometry is reconstructed, computational domain is defined and discretized in smaller sub-domains obtaining the so-called mesh (a grid of elements). During the solving stage, the user selects properties that best describe the fluid behavior and provide the proper boundary and initial conditions. After that, the governing equations are solved in the volume of interest using numerical methods such as finite volume method. In this case, the numerical approach provides an approximate solution of the fluid motion and wall transfer of LDL and oxygen under unsteady flow conditions. Lastly, post-processing involves data analysis and visualization of results via plots, surface maps, etc.

This chapter focuses on the first steps of the procedure: preprocessing and simulation while in the next chapter the results obtained from the post-processing will be analyzed.

2.1 Model reconstruction

The 3D geometries of two carotid bifurcations, a right coronary artery and a left coronary artery were reconstructed from medical images. Two different imaging techniques were adopted depending on the arterial district. High-resolution magnetic resonance imaging (MRI) was used to acquire the geometry of the two carotid bifurcations.

MRI scans were performed on a 3 T scanner (Achieva, Philips Healthcare; Best, The Netherlands) using a bilateral four-channel phased-array carotid coil (Pathway MRI; Seattle, WA, USA). Images were acquired from 3D contrast-enhanced magnetic resonance angiography (CE-MRA) and segmented in order to reconstruct the three-

dimensional geometry. As detailed in a previous study [41] the CCA lumen geometry was reconstructed from the thoracic segment, where possible, to above the bifurcation, using the open-source Vascular Modelling Toolkit (VMTK, www.vmtk.org). Then, subject-specific flow rate waveforms at inflow and outflow sections were extracted from phase contrast MRI (PC-MRI) [42].

As regards coronary arteries, the images of the RCA and the LAD arteries were acquired using computed coronary tomography angiography (CCTA) (SOMATOM Force, Siemens Healthcare) and intravascular ultrasound (IVUS) (InfraReDx, Burlington, MA, USA). Then, both CCTA and IVUS images were used to reconstruct the geometry of the anatomical district. In detail, IVUS images were segmented into lumen contours and stacked upon the CCTA centerline. Additional luminal regions proximal to the IVUS segment up to the aorta and at least two diameters distal to the IVUS-based models were segmented using the CCTA images (**Fig. 2.1**) [43].

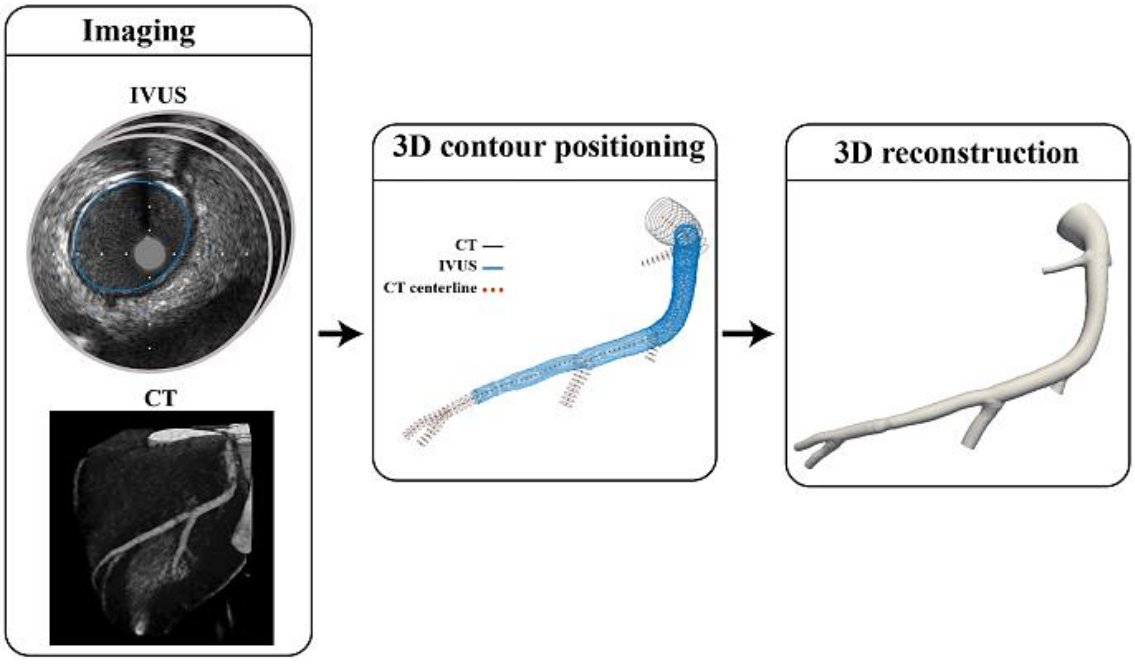

Figure 2.1 Scheme of the coronary arteries geometry reconstruction from medical images.

Computational hemodynamics was performed on each model of carotid and coronary artery (including the side branches) (**Fig. 2.2**). The post-processing was performed in the main branch of the RCA and LAD, and in the carotid bifurcation segment only, i.e., the bifurcation's segment delimited by sections located at 7, 5 and 2 radii along the CCA, ICA and ECA, respectively (denoted as CCA7, ICA5 and ECA2 [41, 37]. The clipping of the side branches was implemented using VMTK (www.vmtk.org) [41].

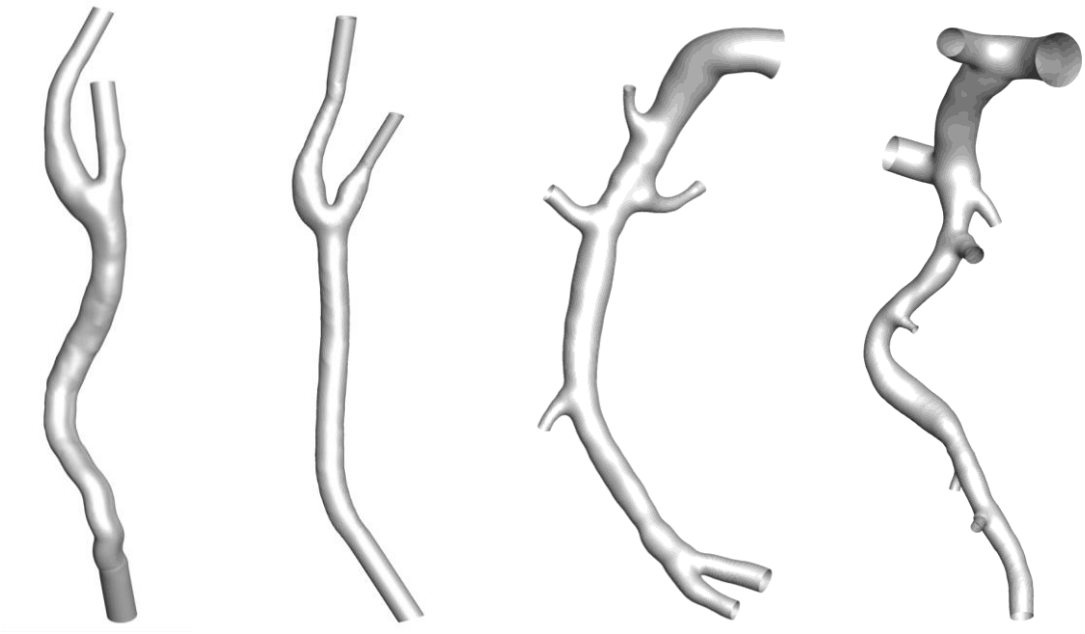

Figure 2.2 Geometry models of the four different anatomical districts investigated: two carotid bifurcations (left) and two coronary arteries (right).

2.2 Model meshing

For the purposes of carrying out the CFD analysis, after the geometry reconstruction, all the reconstructed vessel partitions were discretized. In order to do this, the models were imported into a commercial finite element mesh generator (ICEM, Ansys Inc. USA) [44].

In this study, the same meshing strategy was applied for all models. In detail, an unstructured grid was used for the discretization of the models. Tetrahedral elements were used in the bulk flow while high quality prismatic elements were used to discretize the boundary layer, i.e. the region near the wall (**Fig. 2.3**).

Thus, the fluid domain was divided into about $6 \cdot 10^6$ cells for the first carotid artery, $4.5 \cdot 10^6$ cells for the second carotid artery, $3.9 \cdot 10^6$ cells for the RCA and $3.6 \cdot 10^6$ cells for the LAD. Higher cell density was generated near the wall using 30 layers made up of high-quality prismatic elements for each model.

The choice of using a highly-accurate discretization of the boundary layer was motived by the aim of investigating the transport of LDL and oxygen from the bulk to the wall and their consequent accumulation [45].

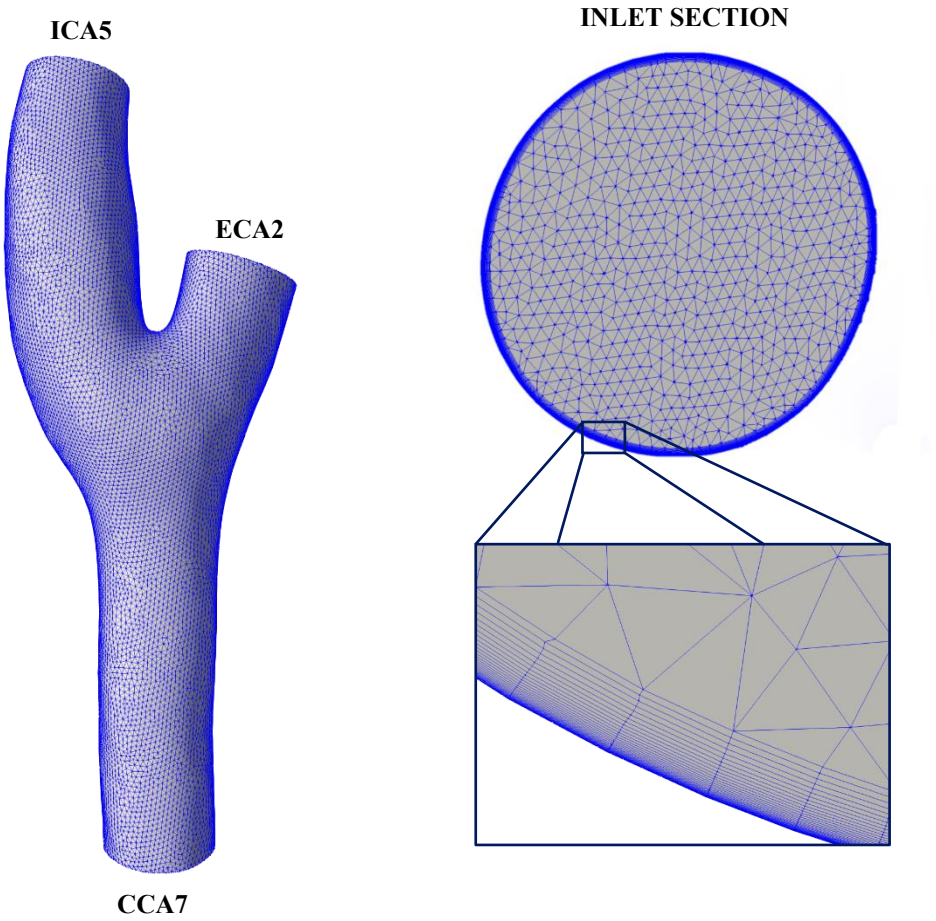

Figure 2.3 3D mesh of a carotid artery involved in the numerical simulation (the full-length model was used to perform CFD). A focus of the boundary layer with its 30 levels in the box.

2.3 Numerical approach

2.3.1 Simplifying assumptions

Before carrying out the numerical simulation, some assumptions and simplifications have been made.

Blood was treated as a homogeneous, isotropic, incompressible, Newtonian viscous fluid with density ρ equal to 1060 kg/m^3 and dynamic viscosity μ set to a constant value of 3.5 cP (0.0035 Pa·s).

Considering each component of the stress tensor τ as a linear isotropic function of the velocity gradient $(\nabla \boldsymbol{u})$ components, the following expression is valid for an incompressible fluid:

$$\boldsymbol{\tau} = 2\mu \boldsymbol{D}(\boldsymbol{u}) \tag{1}$$

where $\boldsymbol{D}(\boldsymbol{u})$ is the rate of deformation tensor. Since the shear rate $\dot{\boldsymbol{\gamma}}$,which is also the gradient of the velocity vector, is related to the second invariant of $\boldsymbol{D}$, equation (2) explains that, for a Newtonian fluid, there is a linear relation between shear stress and shear rate and the shear stress is directly proportional to the shear rate through the definition of a constant which is the dynamic viscosity of the fluid (μ), as shown by the following equation:

$$\boldsymbol{\tau} = \mu \dot{\boldsymbol{\gamma}} \tag{2}$$

The blood, due to its complex nature, can't strictly be treated homogeneous with a Newtonian rheological behaviour. However, these assumptions could be considered acceptable and helpful when it comes to great vessels and high shear rates. If these two conditions are both verified, considering blood as a homogeneous and Newtonian fluid is a valid simplification.

In fact, in great diameter blood vessels (more than 0.3 mm of cross section diameter) the characteristic dimension of red blood cells is at least two orders of magnitude smaller than the vessel diameter itself. Instead, as regards small diameter blood vessels (less than 0.3 mm of cross section diameter) the characteristic dimension of red blood cells becomes comparable with the diameter of the vessel and the hypothesis above does not allow a sufficiently correct evaluation of the fluid dynamic phenomena that take place in the vessel itself. In this case, more complex rheological models are needed in order to take into account the cellular components.

Moreover, in vessels exposed to low shear rates (less than 100 s^{-1}) the dynamic viscosity becomes a function of other parameters. Red blood cells tend to aggregate forming bigger structures called *rouleaux*. These stacks of erythrocytes, due to their dimensions, offer a greater resistance to blood streaming, increasing the viscosity. In this case, blood tends to behave in a non-Newtonian way (as a pseudoplastic fluid).

In this work, considering the anatomical districts involved, all the assumptions and simplifications mentioned so far, have been considered acceptable.

With regards blood flow, it was considered to be laminar. Generally, different fluid flow conditions can be characterized using the dimensionless parameter known as Reynolds number (Re), which, for flow in a pipe, is defined as:

$$Re = \frac{\rho v D}{\mu} \tag{3}$$

where v is the mean velocity of the fluid, ρ the density of the fluid (in this case is the blood), μ the fluid dynamic viscosity and D is the hydraulic diameter of the pipe (in this case D is the diameter of the cross section of the carotid and coronary arteries). From a physical point of view, Reynolds number represents the ratio between the contribution of inertial forces ($\rho v D$) and the contribution of viscous forces (μ). According to Reynolds number, fluid motion in a pipe can be classified in *laminar flow*, *transitional flow* and *turbulent flow*. Laminar flow occurs at low Reynolds numbers ($Re < 2000$): the viscous forces dominate, thus flow appears organized, with no mixing and with each fluid layer slide over the adjacent one. Transitional flow ($2000 < Re < 10000$) is a mixture of laminar and turbulent flow, viscous and inertial forces are significantly unbalanced. Turbulent flow occurs at high Reynolds numbers ($Re > 10000$): inertial forces are dominant and flow is characterized by chaotic structures such as eddies or vortices.

In this work, it was observed that the hemodynamic of the carotid arteries and coronary arteries is characterized by a mean Reynolds number lower than 2000 at the inlet section. Blood flow can destabilize in the systolic phase only, reaching Reynolds number higher than 2000, but, even in this case, there is a too short period for the flow to fall in the turbulent regime. For this reason, considering laminar flow is a valid assumption for the case under investigation.

Lastly, arterial wall was assumed to be rigid with no-slip conditions at the wall and straight flow extensions were matched to the outlet sections of all models to ensure a fully developed flow and to minimize the influence of the boundary conditions on the results [43].

2.3.2 Fluid dynamic problem formulation

This paragraph focuses on the formulation of the mathematical problem for the hemodynamics modelling. Governing equations of the fluid motion are the *Navier-Stokes* momentum equation and the continuity equation, written as follows:

$$\begin{cases} \dfrac{\partial(\rho \boldsymbol{u})}{\partial t} + \nabla \cdot \rho \boldsymbol{u}\boldsymbol{u} + \nabla p = \nabla \boldsymbol{\tau} + \rho \boldsymbol{f_v} & (4) \\ \dfrac{\partial \rho}{\delta \tau} + \nabla \cdot (\rho \boldsymbol{u}) = 0 & (5) \end{cases}$$

The term $\boldsymbol{u}$ represents the fluid velocity vector, p is the pressure, ρ is the fluid density and $\rho \boldsymbol{f_v}$ is the term related to the volume forces.

The Navier-Stokes equations arise from the momentum and mass conservation according to a Eulerian approach, (the computational domain represents a specific location in the space, through which the fluid flows as time passes).

The momentum conservation can be expressed as follows:

$$\begin{pmatrix} rate\ of \\ momentum \\ accumulation \\ in\ the\ control \\ volume\ CV \end{pmatrix} = \begin{pmatrix} rate\ of \\ momentum \\ entering\ CV \end{pmatrix} - \begin{pmatrix} rate\ of \\ momentum \\ leaving\ CV \end{pmatrix} + \begin{pmatrix} resulting\ of \\ forces\ acting \\ on\ the\ system \end{pmatrix}$$

This expression states that the variation in time of momentum inside the control volume is a summation of the ingoing momentum flow, the outgoing momentum flow and the resulting of forces acting of the system.

According to the mass conservation, instead, the variation in time of mass inside the control volume equals the sum of ingoing mass flow and outgoing mass flow:

$$\begin{pmatrix} rate\ of \\ mass\ accumulation \\ in\ the\ control\ volume\ CV \end{pmatrix} = \begin{pmatrix} rate\ of \\ mass \\ entering\ CV \end{pmatrix} - \begin{pmatrix} rate\ of \\ mass \\ leaving\ CV \end{pmatrix}$$

Assuming that the blood is an incompressible fluid with a Newtonian behavior, the density ρ is considered constant and the term $\nabla\boldsymbol{\tau}$ becomes $\mu\nabla^2\rho$, where the dynamic viscosity μ is set to a constant value equal to 3.5 cP. Thus, the Navier-Stokes equations, for an incompressible Newtonian fluid become:

$$\begin{cases} \rho\left[\dfrac{\partial \boldsymbol{u}}{\partial t} + \boldsymbol{u}(\nabla \cdot \boldsymbol{u})\right] = -\nabla p + \mu\nabla^2\boldsymbol{u} + \rho g & (6) \\ \nabla \cdot \boldsymbol{u} = 0 & (7) \end{cases}$$

where the term related to the volume forces $\rho\boldsymbol{f_v} = \rho g$.

Since Navier-Stokes equations are non-linear partial differential equations, where the unknown variables are the blood velocity vector $\boldsymbol{u}$ and the pressure p, finding an analytical solution is typically an impossible task. For this reason, a discretized version of these equations can be solved in the investigating domain by means of computational methods.

The investigating fluid domain **Ω** is represented by the lumen of the vessel (in this case the vessels are two carotid arteries and two coronary arteries) and the vessels walls together with the inlet and outlet sections represent the boundary of the domain, namely Γ^w, Γ^{in} and Γ^{out}, respectively (**Fig. 2.4**). All CFD simulations were carried out in FLUENT (ANSYS Inc., USA), using the finite volume method.

2.3.3 LDL transport problem formulation

To model the mass transport of LDL particles in the streaming blood, the governing equations of fluid motion (6, 7) were coupled with the advection-diffusion equations under unsteady flow conditions.

In detail, LDL, assumed to be present in dissolved form in blood, was modelled as a passive non-reacting scalar transported in the streaming blood by means of the advection-diffusion equation:

$$\frac{\partial C}{\partial t} + \boldsymbol{u} \cdot \nabla C - D_{LDL} \nabla^2 C = 0 \tag{8}$$

In equation (8), C is the LDL concentration in blood, $\boldsymbol{u}$ is the velocity vector of the fluid and D_{LDL} is the LDL diffusivity in the streaming blood, set to $6.3 \cdot 10^{-9}\, kg/ms$. The non-stationary or transient term is $\frac{\partial C}{\partial t}$ that represents the non-stationarity of the system (the hypothesis of pulsatile blood flow was considered), $\boldsymbol{u} \cdot \nabla C$ represents the advective/convective term which describes the change in LDL concentration at a given location because of the flow and $-D_{LDL} \nabla^2 C$ is the diffusive term and describes the transport of LDL in streaming blood due to diffusion (proportional to the Laplacian, or second derivative, of concentration C).

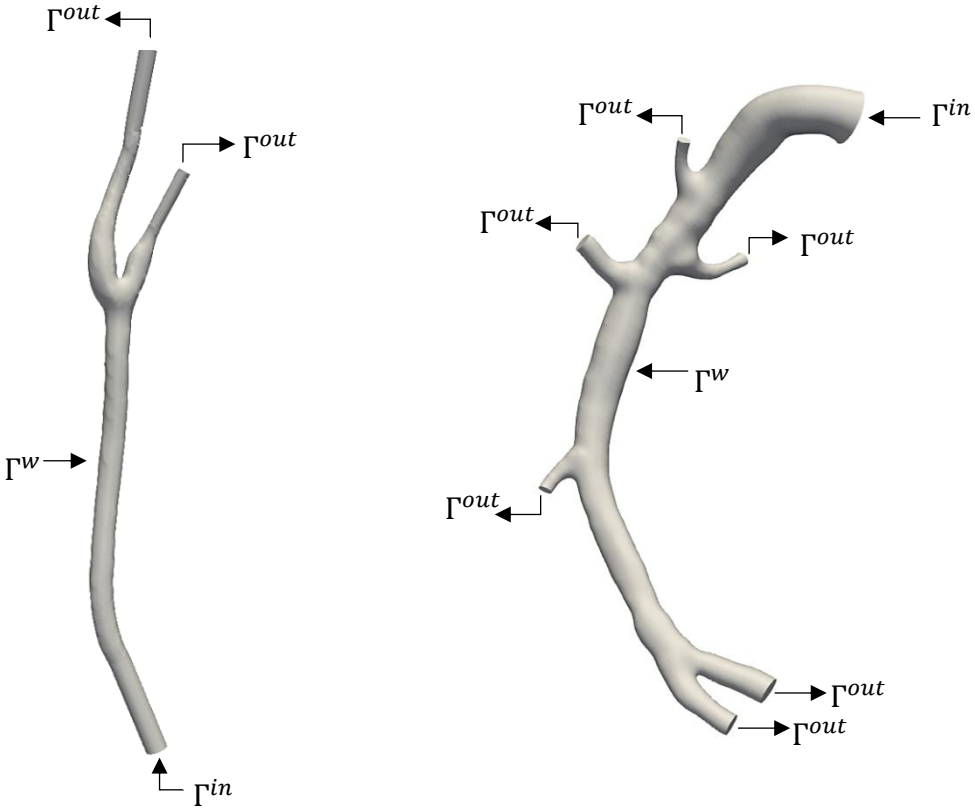

Figure 2.4 Detail of domain boundary with Γ^{w}, Γ^{in} and Γ^{out} for a carotid artery and the right coronary artery.

To implement mass transport in FLUENT, it is necessary to define the so-called *User-Defined Scalar (uds)* since the LDL concentration (C) is considered by the software as a scalar that diffuses in the domain of interest (blood). In this case, the *uds* is defined

as the ratio C/C_0 between the LDL concentration at a given location and the average LDL concentration in whole blood (C_0). The accumulation of LDL at the vessel wall was evaluated in terms of normalized LDL concentration, i.e. C/C_0.

2.3.4 Oxygen transport problem formulation

Oxygen transport in streaming blood consists of two contributions: oxygen carried by hemoglobin and free oxygen dissolved in blood. In this work, both contributions were simulated. Also in this case, oxygen was modelled as a passive non-reacting scalar transported in the streaming blood by means of the relative advection-diffusion equation:

$$\frac{\partial PO_2}{\partial t} + \left(1 + \frac{[Hb]}{\alpha}\frac{dS}{dPO_2}\right)\boldsymbol{u}\cdot\nabla PO_2 - \nabla\cdot\left[D_b\left(1 + \frac{[Hb]}{\alpha}\frac{D_c}{D_b}\frac{dS}{dPO_2}\right)\nabla PO_2\right] = 0 \tag{9}$$

where $[Hb]$ is the total oxygen carrying capacity of hemoglobin in blood set to 0.2 mL O_2/mL blood; α is the solubility of oxygen in plasma equal to 2.5×10^{-5} mL O_2/mL blood/mmHg; $\boldsymbol{u}$ is the velocity vector of the fluid; PO_2 is the plasma oxygen partial pressure or tension. D_b represents the diffusivity of the free oxygen in blood ($D_b = 1.2 \times 10^{-9}\, m^2/s$) and D_c represents the diffusivity of oxyhemoglobin in blood ($D_c = 1.5 \times 10^{-11}\, m^2/s$). The saturation function S, defined as the ratio of oxyhemoglobin to total hemoglobin, has been approximated by the Hill equation:

$$S = \frac{PO_2^n}{PO_2^n + PO_{50}^n} \tag{10}$$

where $n = 2.7$ and $PO_{50}^n = 26.6$ mmHg [46, 57]. PO_{50} is the partial pressure of oxygen at which hemoglobin is 50% saturated.

Due to the non-linear nature of eq. (9), the numerical solution is computationally intensive. Therefore, the following linearization has been applied [57]:

$$\frac{dS'}{dPO_2} = \frac{nS'}{PO_2'}(1 - S') \tag{11}$$

where PO_2' is a reference value of PO_2 set to 75 mmHg and S' is S evaluated at PO_2'.

Referring to equation (9), the first two terms represent, respectively, the non-stationary term and the advection term, while the last one is the diffusion term. The coefficient $\left(1+\frac{[Hb]}{\alpha}\frac{dS}{dPO_2}\right)$ can be interpretated as a non-constant oxygen carrying capacity, while the term $D_b\left(1+\frac{[Hb]}{\alpha}\frac{D_c}{D_b}\frac{dS}{dPO_2}\right)$ represents a non-constant diffusivity. The approximation (11) was used to linearize both the second and the third term of equation (9), resulting in a constant diffusivity value in the whole domain $\left(D=D_b\left(1+\frac{[Hb]}{\alpha}\frac{D_c}{D_b}\frac{dS\prime}{dPO_2'}\right)=1.4337\times10^{-9}\,m^2/s\right)$.

As the LDL transport, to implement oxygen transport in FLUENT it is necessary to define the *User-Defined Scalar (uds).* In this case the *uds* is defined as the plasma oxygen tension (PO_2). Then, the oxygen flux at the wall is evaluated through the non-dimensional Sherwood number, computed from PO_2.

The Sherwood number represents the ratio between the convective and diffusive contribution of the oxygen transport and it is described by the following equation:

$$Sh = k\frac{a}{D} \tag{12}$$

where k is the oxygen mass transfer coefficient, a is the vessel diameter and D is the oxygen diffusivity in plasma, given by the two contributions D_b and D_c. In detail, k can be expressed as follows:

$$k = \frac{-D\left.\frac{\partial PO_2}{\partial n}\right|_{wall}}{PO_{2\,inlet} - PO_{2\,wall}} \tag{13}$$

where $\left.\frac{\partial PO_2}{\partial n}\right|_{wall}$ is the PO_2 gradient in the normal direction to the wall, whereas data from literatures were adopted for $PO_{2\,inlet}$ and $PO_{2\,wall}$ as described later [55].

The Sherwood number gives an idea about the oxygen concentration near the wall. Low Sh values indicate a hypoxic condition, linked to the onset or development of atherosclerosis.

For this thesis, oxygen transport was simulated only for the RCA and the Carotid 2 models.

2.3.5 Boundary conditions

In order to close the problem and solve the equations above-mentioned, a series of boundary conditions (BCs) was prescribed on the border $\partial\Omega$ of the investigating domains.

As regards the carotid arteries, the border consists of three different surfaces: Γ^{w}, Γ^{in} and two Γ^{out}. Γ^{w} refers to the border represented by the vessel wall while Γ^{in} and Γ^{out} represent the inlet and the outlet surfaces of the model, which are fictitious surfaces obtained clipping the model perpendicularly to the vessel centerlines, thus separating the artery from the rest of the circulatory system. In particular, Γ^{in} corresponds to the CCA inlet (or inflow boundary) and Γ^{out} denotes the outlets (or outflow boundaries), which, for the carotid model, are the internal carotid artery (Γ^{ICA}) and the external carotid artery (Γ^{ECA}).

In the same way, the border of the right coronary artery consists of eight different surfaces: Γ^{W}, Γ^{in} and six Γ^{out}. The outlets were obtained again by cutting the five side branches, denoted as SB1 (Γ^{SB1}), SB2 (Γ^{SB2}), SB3 (Γ^{SB3}), SB4 (Γ^{SB4}) and SB5 (Γ^{SB5}), As for LAD, the seven side branches were cut in order to obtain the respective outlets: SB1 (Γ^{SB1}), SB2 (Γ^{SB2}), SB3 (Γ^{SB3}), SB4 (Γ^{SB4}), SB5 (Γ^{SB5}), SB6 (Γ^{SB6}) and SB7 (Γ^{SB7}).

2.3.5.1 BCs for fluid dynamics

In this paragraph, the BCs strategies for the fluid dynamic problem applied both at the carotid and coronary arteries are illustrated.

At the border Γ^{W}, which represents the vessel wall, the condition of perfect adherence of the fluid particles to the wall, which is assumed as rigid, is imposed, i.e. a Dirichlet condition:

$$\boldsymbol{u} = 0 \qquad on\ \Gamma^{W}$$

Then, patient-specific boundary conditions were prescribed at the inlet and outlet sections to numerically solve the Navier-Stokes equations. More in detail, measured 3D flow rates (using PC-MRI for carotid arteries and ComboWire Doppler measurements for coronary arteries) were applied as inflow boundary conditions at the inlet section of each model in terms of time-dependent flat velocity profiles.

The strategy applied at the outflow boundaries of the coronary arteries consists in the application of fixed flow rate ratios, i.e. the ratio between the average flow rate at each outlet of the districts and the average flow rate at the corresponding inlet sections. Flow rate ratios can be measured or estimated (if in vivo measurements are unavailable or inaccurate).

As regards the two carotid arteries, a measured flow-rate was applied at the ICA outlet and a traction-free condition was used at the ECA outlet.

2.3.5.2 BCs for LDL mass transport

The LDL mass transport equation was solved both in the carotid and coronary arteries by imposing the following boundary conditions:

$$\text{I.} \quad \text{BC } \textit{inlet}: C = C_0 \tag{14}$$

$$\text{II.} \quad \text{BC } \textit{outlets}: \frac{\partial C}{\partial n} = 0 \tag{15}$$

$$\text{III.} \quad \text{BC } \textit{wall}: D_{LDL} \left.\frac{\partial C}{\partial n}\right|_{wall} = C_w v_W \tag{16}$$

The boundary condition for LDL transport applied on the inlet section Γ^{in} (14) assumes a specified constant value of the LDL concentration, which is the same as the LDL mean concentration in the bulk flow ($C_0 = 2.86 \cdot 10^{-9}\, mol/m^3$) [47]. As regards all the outlets of each model, equation (15) implies that LDL concentration gradient in the direction normal to the outlet section, is assumed to be zero (stress-free condition). LDL transfer across the arterial wall was modelled using the equation (16), where C_w is the concentration of LDL at the arterial wall, v_W is the water filtration velocity through the wall considered to be $4 \cdot 10^{-8}\ m/s$ according to literature data, D_{LDL} is the LDL diffusivity, n is the direction normal to the boundary (in this case the wall) and $\left.\frac{\partial C}{\partial n}\right|_{wall}$ is the gradient of LDL concentration in the direction normal to the wall. This equation is a

balance between the amount of LDL carried to the arterial wall by the water filtration flow (right side of the equation) and the amount of LDL that diffuses back to the bulk flow (left side of the equation).

The equation (16) arises from a more general equation:

$$C_w v_W - D_{LDL} \frac{\partial C}{\partial n}\Big|_{wall} = K_w C_W \tag{17}$$

in which K_w, representing the permeability coefficient of LDL at the vessel wall, was assumed to be 0 [48, 49].

Technically, this equation, in its simplified form, was implemented in FLUENT as a validated C-like function, called *User-Defined Function (udf)*.

2.3.5.3 BCs for oxygen mass transport

Also the oxygen mass transport equation was solved both in the carotid and coronary arteries by imposing the following boundary conditions:

I. BC *inlet*: $PO_{2\,inlet} = 85\ mmHg$ (18)

II. BC *outlets*: $\frac{\partial PO_2}{\partial n} = 0$ (19)

III. BC *wall*: $PO_{2\,wall} = 60\ mmHg$ (20)

Literature data were considered in order to impose the boundary conditions for oxygen transport on the inlet section Γ^{in} (18) and on the arterial wall Γ^{wall} (20) [46]. As LDL mass transport, equation (19) implies a null transfer of the scalar PO_2 in the direction normal to the outlet section (stress-free condition).

2.3.6 Initial conditions

In addition to the boundary conditions described previously, initial conditions were imposed for the LDL and oxygen distributions. In detail, these initial conditions are the same for both carotid and coronary arteries.

As for LDL, the imposed initial condition consists in the initialization of the LDL concentration to a uniform and constant value ($C_0 = 2.86 \cdot 10^{-9}\ mol/m^3$) in the whole

domain. As regards the oxygen, just like LDL particles, a uniform and constant plasma oxygen tension ($PO_{2\ inlet} = 85\ mmHg$) throughout the domain was imposed as initial condition (**Fig. 2.5**).

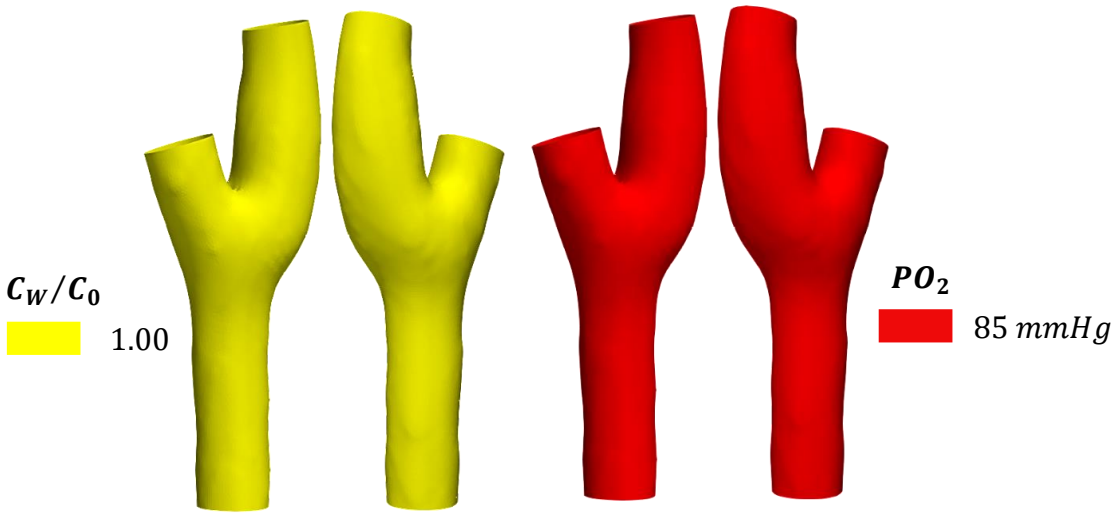

Figure 2.5 Initial uniform conditions for LDL (left) and oxygen (right) transport detailed for a representative model of carotid artery.

2.4 Post-processing

To analyze the hemodynamics at the wall, features of the WSS vector field were analyzed. First, the classical descriptors of the WSS were calculated, i.e. TAWSS, OSI, RRT, transWSS (detailed later). Then, a new hemodynamic descriptor, based on WSS divergence, has been investigated. For the purpose of evaluating the ability of these parameters to provide a template of the wall mass transfer of LDL and oxygen particles, a co-localization analysis has been conducted.

2.4.1 WSS-based descriptors

Several hemodynamic wall descriptors have been proposed over the years to quantify hemodynamic disturbances as a potential predictors of vascular wall dysfunction [50].

The first classical WSS-based descriptor introduced in this work is the *Time-Average Wall Shear Stress (TAWSS)*:

$$TAWSS = \frac{1}{T}\int_0^T |WSS(s,t)| \cdot dt \tag{21}$$

where $WSS(s,t)$ is the WSS vector as a function of space s and time t, and T is the period of the cardiac cycle.

The Time-Averaged Wall Shear Stress represents the change in modulus of WSS mediated over a cardiac cycle. Low TAWSS values (lower than 0.4 Pa) are known to stimulate a proatherogenic endothelial phenotype; moderate TAWSS values (between 1.5 Pa and 10 Pa) induces endothelial quiescence and an atheroprotective gene expression profile [51, 52] and higher TAWSS values (greater than 10-15 Pa) can lead to endothelial trauma and hemolysis [53].

Since TAWSS does not consider the direction of the flow, another descriptor was introduced, the *Oscillatory Shear Index (OSI)* [58]:

$$OSI = 0.5\left[1 - \left(\frac{\left|\int_0^T WSS(s,t) \cdot dt\right|}{\int_0^T |WSS(s,t)| \cdot dt}\right)\right] \qquad 0 \leq OSI \leq 0.5 \tag{22}$$

OSI is a dimensionless parameter which represents the oscillatory behaviour of the WSS over a cardiac cycle. It is used to identify regions on the vessel wall subjected to highly oscillating WSS values, usually associated with bifurcations and vortex formation that may induce atherosclerotic plaque formation. OSI values close to 0.5 imply an oscillatory behaviour WSS with a consequent proatherogenic role, while OSI values close to 0 indicate a unidirectional, more physiological, WSS.

A summary of the meaning of the two previous descriptors is reported in the *Relative Residence Time (RRT)* [59]:

$$RRT = \frac{1}{(1 - 2 \cdot OSI) \cdot TAWSS} = \frac{T}{\left|\int_0^T WSS(s,t) \cdot dt\right|} \tag{23}$$

This descriptor provides a measure of low and oscillatory WSS and indicates how long the atherogenic particles remain near the vessel wall. High RRT values, which correspond to low TAWSS and high OSI, indicate a potential zone of atherosclerotic plaque formation.

To account for the multidirectional nature of WSS, a new descriptor, called *transverse Wall Shear Stress (transWSS)*, was introduced [60]:

$$transWSS = \frac{1}{T}\int_0^T \left| WSS(s,t) \cdot \left(n \times \frac{\int_0^T WSS(s,t) \cdot dt}{\left|\int_0^T WSS(s,t) \cdot dt\right|} \right) \right| \cdot dt \qquad (24)$$

where n represents the normal to the arterial surface. This metric is able to capture the multidirectionality of the instantaneous WSS. Basically, high transWSS values indicate large changes in flow direction.

2.4.2 WSS topological skeleton

As stated before, a marked interest has recently emerged on WSS topological skeleton, due to its ability to strictly reflect the presence of near-wall hemodynamic features associated with vascular disease.

The WSS topological skeleton consists of fixed points and manifolds. The former are critical points where the WSS vector vanishes, while manifolds are expansion/contraction regions linking fixed points. The nature of a fixed point can be either stable or unstable. A stable point attracts all trajectories that start close to it, while an unstable point repels trajectories starting close to it. Moreover, a fixed point can be classified as a node, a focus or a saddle point, as detailed in [35] (**Fig. 2.6**).

Nowadays two approaches are proposed in literature to analyze the features of the WSS topological skeleton, i.e. the Lagrangian and Eulerian ones. The Lagrangian-based analysis, proposed by Arzani and coworkers is based on the study of the *Lagrangian Coherent Structures (LCS)* as detailed in [54]. This kind of analysis requires high computational costs and has a difficult implementation. To overcome these limitations, a Eulerian method to analyze the WSS topological skeleton has been recently proposed [35].

Based on the Volume Contraction Theory it was demonstrated that the calculation of the normalized WSS vector field divergence allows to identify the WSS topological skeleton features on the luminal surface of a vessel. The divergence of the WSS field gives physical information about the events at the interface blood - vessel wall: (1) a local positive value of the WSS divergence at the luminal surface means that locally shear

forces exert an expansion action on the endothelial cells; (2) a local negative value of the WSS divergence at the luminal surface means that locally shear forces exert a contraction action on the endothelial cells [56].

In this study, the divergence of the normalized cycle-average WSS vector field was computed in order to identify expansion/contraction regions. The divergence of the normalized WSS vector field can be expressed as:

$$DIV_W = \nabla \cdot (WSS_{\boldsymbol{u}}) = \nabla \cdot \left(\frac{WSS}{\|WSS\|}\right) \tag{25}$$

where $WSS_{\boldsymbol{u}}$ is the WSS unit vector.

Luminal surface regions characterized by positive values of DIV_W identify expansion regions and approximate stable manifolds, while luminal surface regions where DIV_W has a negative value identify contraction regions and approximate unstable manifolds [34, 56].

To complete the WSS topological skeleton analysis fixed points were identified by computing the Poincaré index and then classified using the eigenvalues of the Jacobian matrix of the WSS vector field (**Table 1**).

Fixed points	***Eigenvalues***	***Poincaré index***
Unstable node	$\lambda_1 > \lambda_2 > \lambda_3 > 0$	1
Stable node	$\lambda_1 < \lambda_2 < \lambda_3 < 0$	1
Saddle point	$\lambda_1 < \lambda_2 < 0 < \lambda_3$	-1
Saddle point	$\lambda_1 > \lambda_2 > 0 > \lambda_3$	-1
Unstable focus	$\lambda_1 > 0, \lambda_{2,3} = \alpha \pm \beta i$	1
Stable focus	$\lambda_1 < 0, \lambda_{2,3} = -\alpha \pm \beta i$	1

Table 1 Identification and classification of fixed points.

The link between WSS topological skeleton and vascular disease is provided by studies documenting a focal response of the endothelial cells to low WSS magnitude (and a fixed point is a point where WSS vector field vanishes) and WSS oscillatory patterns.

Moreover, evidences underline the capability of the WSS topological skeleton to

identify the biochemical concentration patterns at the arterial luminal surface of, e.g., LDL or oxygen, which are involved in the atherogenic process [35, 56]. Results by previous studies show a marked co-localization between high LDL (and low oxygen) luminal concentration and WSS contraction regions, thus confirming the existing link between unstable manifolds and vascular dysfunction.

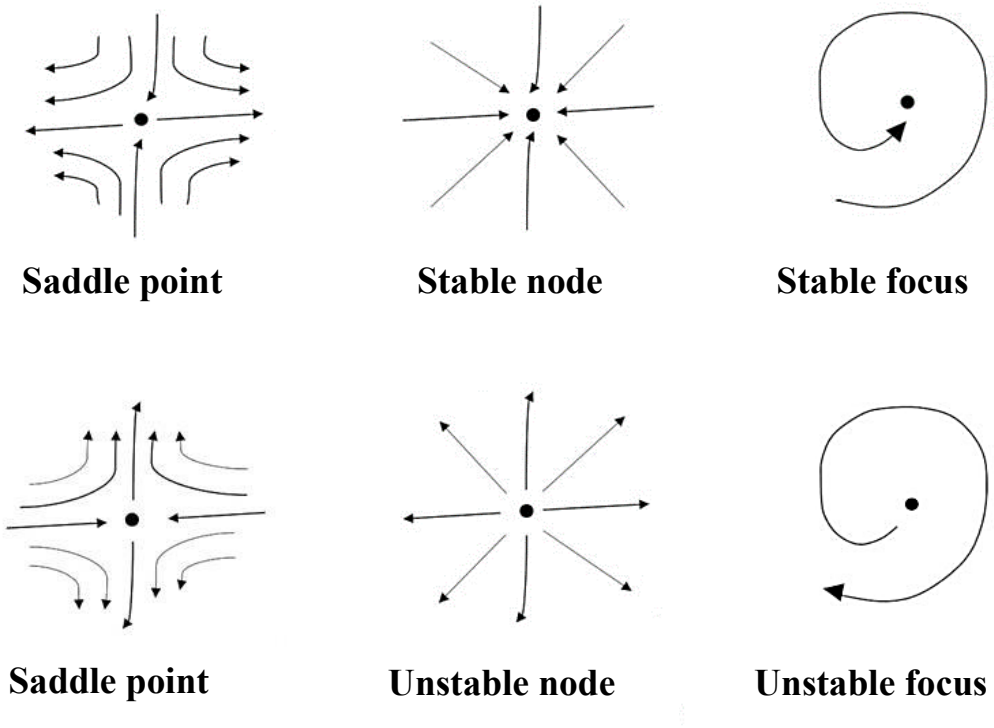

Figure 2.6 Classification of fixed points in a vector field.

2.4.3 Co-localization analysis

To be able to analyze the co-localization existing between zones with disturbed hemodynamics (identified by the classical WSS-based descriptors), WSS contraction regions and LDL/oxygen polarization zones, objective thresholds were computed for each vascular district investigated. More in detail, since critical regions are associated with low TAWSS, DIV, Sh values and high OSI, RRT, transWSS, LDL values, the 10^{th} percentile of the TAWSS, DIV and Sh distributions and the 90^{th} percentile of OSI, RRT, transWSS and LDL distributions were calculated. Thus, the surface area exposed to TAWSS, DIV and Sh values lower than 10^{th} percentile was identified as TAWSS10, DIV10 and SH10, respectively. In the same way, the surface area exposed to OSI, RRT,

transWSS and LDL values higher than 90th percentile was denoted as OSI90, RRT90, trans90 and LDL90, respectively.

First, qualitative comparisons were made up by plotting several maps, showed in the next chapter.

Quantitative comparisons were carried on by computing the so-called Similarity Index. The Similarity Index (SI) quantifies the spatial overlap of the surface areas exposed to LDL90 (and SH10) and one of the hemodynamic descriptors (TAWSS, OSI, RRT and DIV) below or above their threshold values. The SI, calculated between two parameters i and j, is described by the following equation:

$$SI = \frac{2\left(SA_i \cap SA_j\right)}{SA_i + SA_j} \tag{26}$$

where SA_i and SA_j represent, respectively, the surface areas exposed to the $i\text{-}th$ and the $j\text{-}th$ generic descriptor above or below the relative threshold value.

The Similarity Index can range between 0 and 1: $SI = 0$ indicates that the two regions are completely disjointed, whereas $SI = 1$ implies a full, perfect co-localization.

Chapter 3

3 Results

In this chapter, all the obtained results, in terms of LDL/oxygen concentration, WSS topological skeleton distribution and co-localization analysis for each investigated model are presented.

3.1 LDL and oxygen surface concentration

This paragraph shows LDL and oxygen concentration at the vessel wall for the four anatomical models investigated.

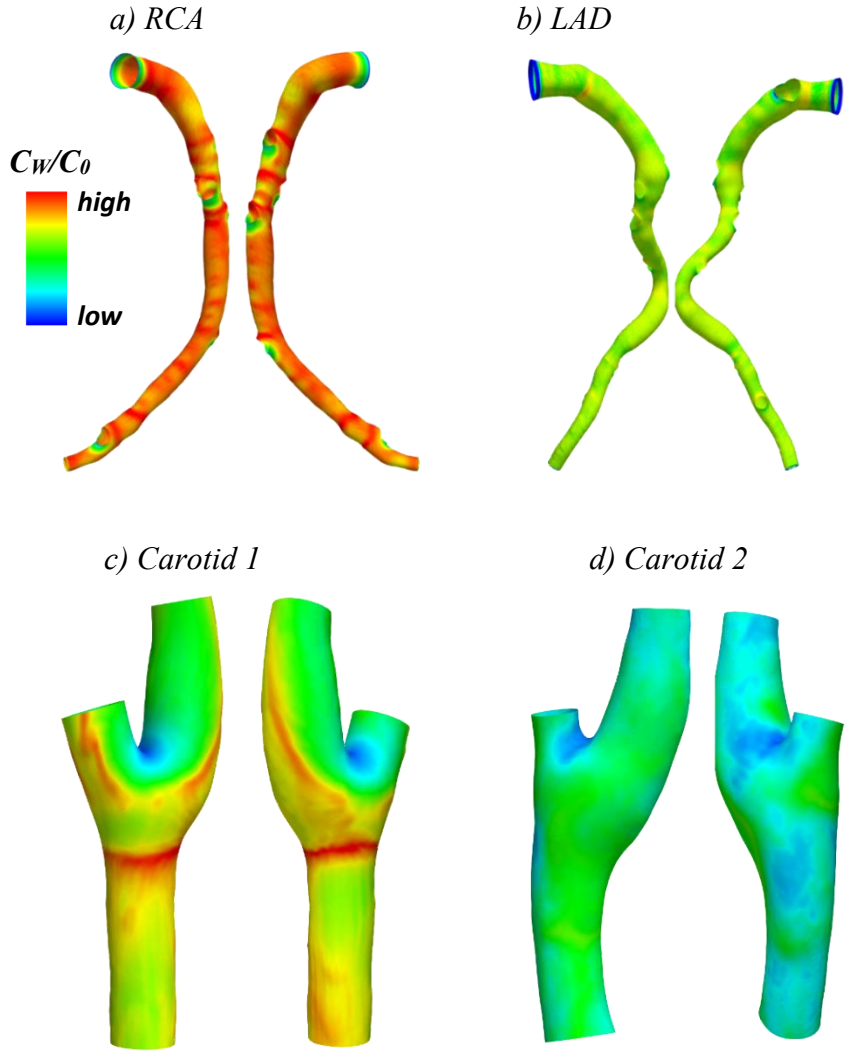

Figure 3.1 LDL concentration at the wall of: a) RCA b) LAD c) Carotid 1 d) Carotid 2.

More in detail, **Fig 3.1** displays LDL concentration at the wall of RCA, LAD, Carotid 1 and Carotid 2. It can be noticed that LDL concentration at the RCA wall is higher than LDL concentration at the LAD wall. In the same way, there is a greater accumulation of LDL at the wall of the Carotid 1, rather than Carotid 2.

A greater accumulation of LDL in the Carotid 1 is observed at the bulb, at the beginning of the bifurcation and along the external walls of the ICA and ECA. As for the two coronary arteries, higher LDL concentration values are located along the inner walls.

Fig. 3.2 shows oxygen concentration at the wall of RCA and Carotid 2 models, in terms of Sherwood number Sh. Here the areas characterized by low Sh are represented in red because hypoxic regions are linked to a high atherogenic risk (just like high LDL regions also represented in red in **Fig. 3.1**).

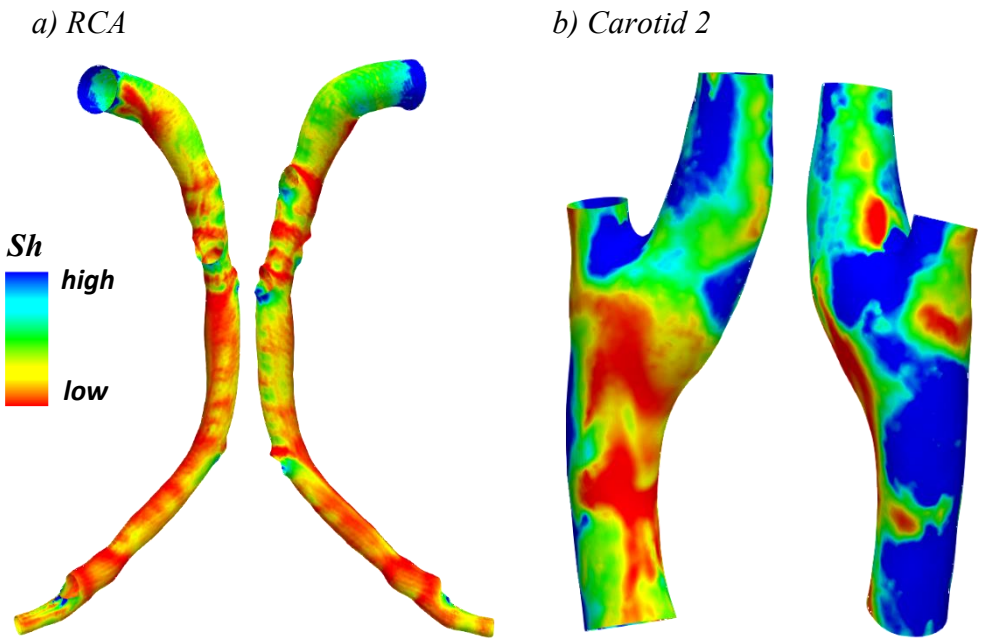

Figure 3.2 Oxygen concentration at the wall of a) RCA and b) Carotid 2.

3.2 WSS topological skeleton analysis

The results related to the Eulerian-based approach used to identify WSS topological skeleton are reported below.

The luminal surface distributions of DIV_W for the four analyzed vascular districts are provided in **Fig. 3.3**. WSS contraction areas are colored in blue, while WSS expansion regions are represented in red color. It emerged that in Carotid 1 a line of marked WSS contraction was located at the base of the carotid bifurcation and along the external walls of the ICA and ECA, as identified by negative DIV values. Moreover, marked expansion zone characterized the WSS topological skeleton on the inner wall of the carotid bifurcation (positive DIV values). Carotid 2 has a fairly similar pattern even if there are more focus/nodes and saddle point than Carotid 1.

As regard RCA, contraction zones are mainly located within the curvature of the vessel and near to the inlet, while, as for LAD, there are two marked contraction lines in the upper part of the vessel (near the inlet). In both coronary arteries critical points are mainly confined to the side branch entrances.

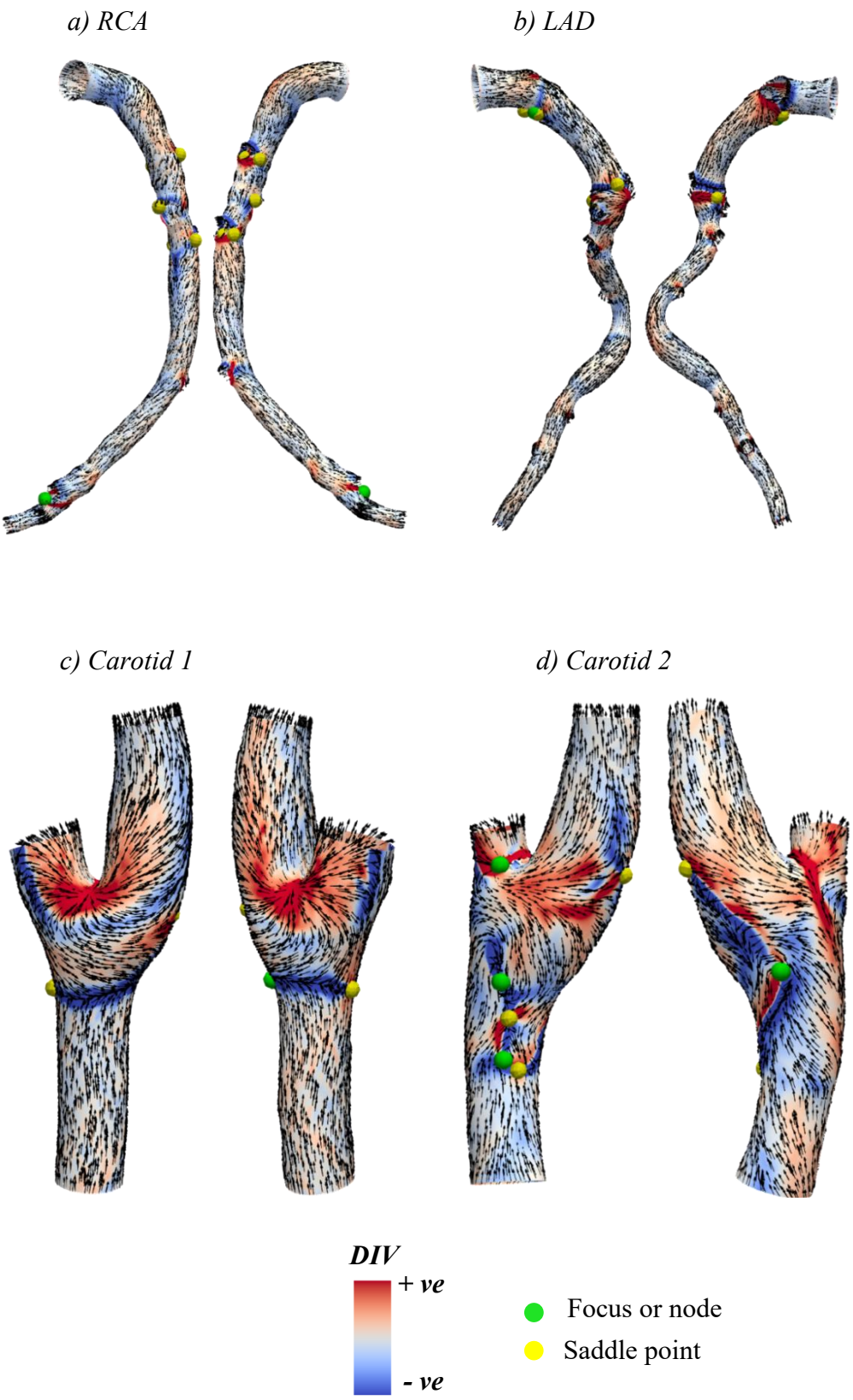

Figure 3.3 WSS topological skeleton of the normalized cycle-average WSS vector field for: a) RCA b) LAD c) Carotid 1 and d) Carotid 2.

3.3 Co-localization results

In order to evaluate the spatial overlap of the hemodynamics descriptors of disturbed shear and WSS contraction/expansion action with LDL/oxygen polarization, a co-localization analysis has been performed for each anatomical district.

Luminal surface areas of LDL90 (yellow-colored regions) and DIV10 (black contour lines) have been graphically overlapped to qualitative appreciate their co-localization (**Fig 3.4**).

It clearly emerges by visual inspection that contraction regions of WSS vector field overlaps with LDL uptake at the vessel wall. The observed co-localization is evident along the inner curvature of the RCA and LAD; at the outer wall of the ICA and ECA of Carotid 1 and at the base of the bifurcation of the two carotid arteries, where is an almost perfect contour of the WSS contraction zones along the LDL polarization areas.
[61]. The co-localization of LDL concentration with WSS contraction regions is less pronounced only locally and it is more evident at the outer wall of Carotid 2.

Fig 3.4 also displays the co-localization analysis conducted between SH10 (red-colored regions) and DIV10 (black contour lines). A very similar pattern can be noticed: also in this case there is a less spatial overlap between oxygen concentration polarization and WSS contraction regions at the outer wall of Carotid 2.

Lastly, a co-localization analysis between LDL90 (yellow-colored regions) and SH10 (red contour lines) has been conducted as shown in **Fig 3.4**. It can be noted that SH10 markedly overlaps with LDL wall concentration, confirming the existing link between LDL polarization areas with hypoxic regions.

The maps in **Fig 3.4** prove the ability of the Eulerian-based WSS topological skeleton analysis to provide an affordable template of the LDL and oxygen concentration polarization at the luminal surface of carotid and coronary arteries [34].

a) RCA

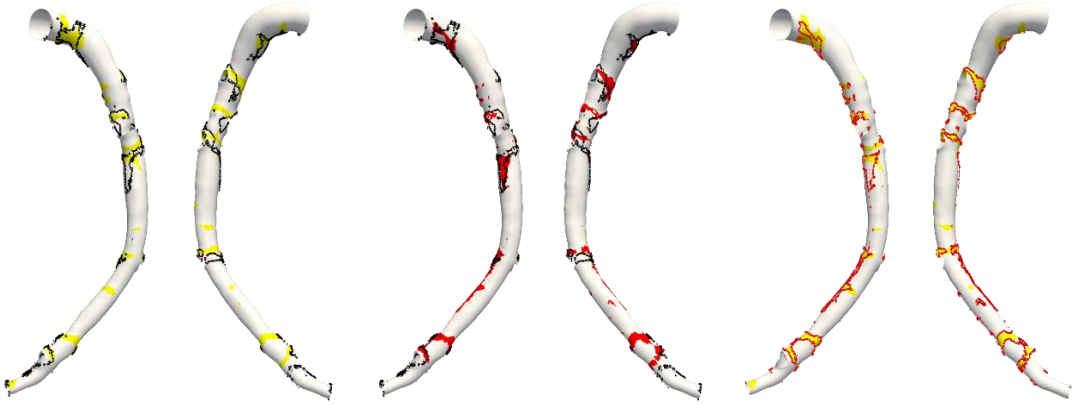

b) Carotid 2

c) LAD

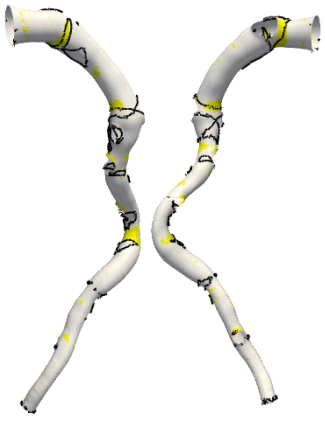

d) Carotid 1

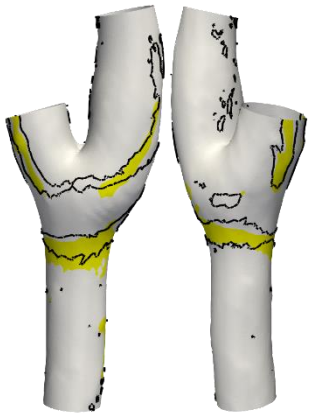

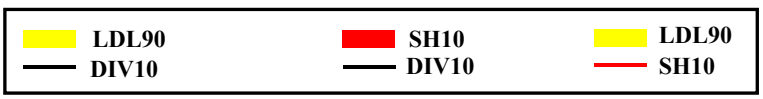

Figure 3.4 Distributions of LDL90-DIV10, SH10-DIV10 and LDL90-SH10 for: a) RCA b) Carotid 2. Distributions of LDL90-DIV10 for: c) LAD and d) Carotid 1.

Then, oxygen polarization at the wall, denoted by SH10, and the distribution of the established WSS-based descriptors (TAWSS10, OSI90, RRT90 and transWSS90) have been graphically overlapped to qualitative appreciate their co-localization (**Fig. 3.5**).

In the same way, the distributions of the established WSS-based descriptors have been graphically overlapped to the luminal surface of LDL90 (**Fig. 3.6**).

By comparing previous images (**Fig. 3.4** Vs. **Fig. 3.5**) it clearly emerges that the co-localization between classical WSS-based descriptors and SH10 is lower than the overlap between DIV10 and SH10. Specially OSI90 and transWSS90 aren't able to catch the oxygen concentration polarization at the vessel wall.

The same goes for the LDL concentration, that is better enclosed by the DIV10 contour rather than the WSS-based descriptors (**Fig. 3.4** Vs. **Fig. 3.6**).

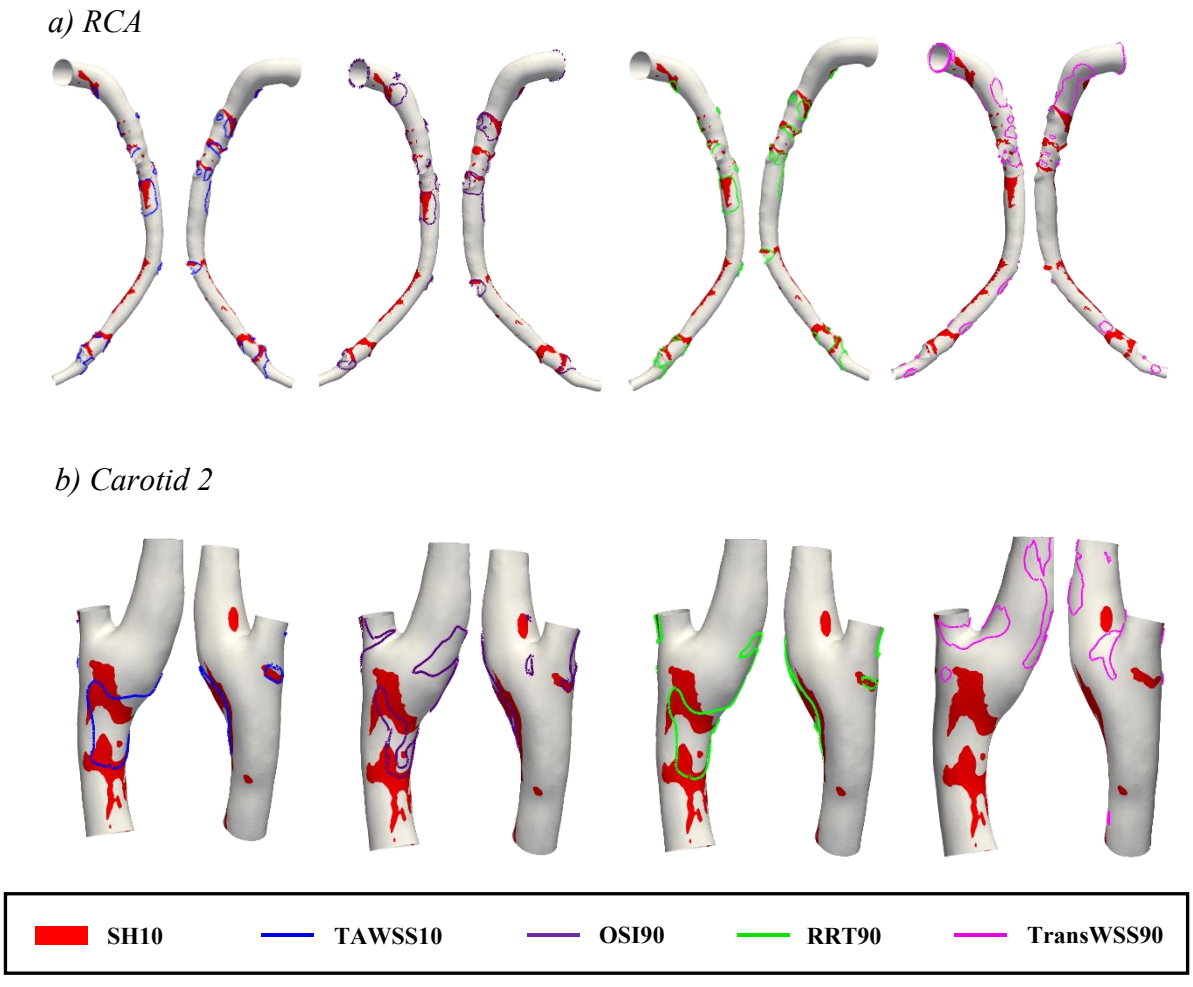

Figure 3.5 Co-localization maps between SH10 and each WSS-based descriptor (i.e. TAWSS10, OSI90, RRT90 and TransWSS90 for a) RCA and b) Carotid 2.

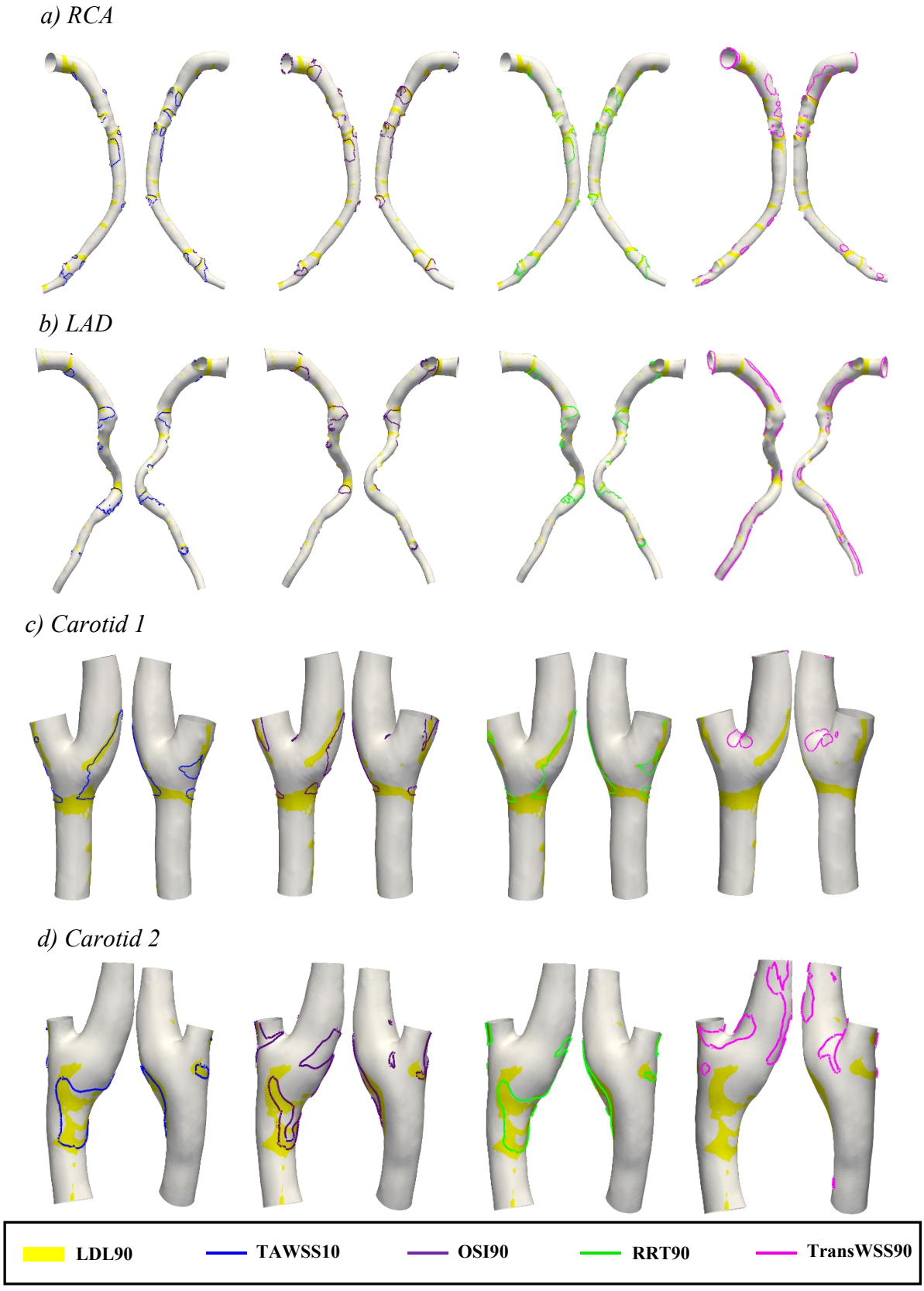

Figure 3.6 Co-localization maps between LDL90 and each WSS-based descriptor (i.e. TAWSS10, OSI90, RRT90 and TransWSS90) for a) RCA b) LAD c) Carotid 1 and d) Carotid 2.

The co-localization has been quantified through the Similarity Index (SI), as shown in the tables below. More in detail, **Table 2** shows the SI between the distribution of hemodynamics descriptors (i.e. TAWSS10, OSI90, RRT90, TransWSS90 and DIV10) and LDL90, for each artery.

	TAWSS10	**OSI90**	**RRT90**	**TransWSS90**	**DIV10**
RCA	0,2329	0,2091	0,2313	0,0056	0,3378
LAD	0,1101	0,1361	0,1289	0,0388	0,1931
Carotid 1	0,2847	0,2244	0,2798	0	0,4812
Carotid 2	0,5385	0,4334	0,5763	$6{,}39 \cdot 10^{-4}$	0,6552

Table 2 Similarity index between LDL90 and each hemodynamics descriptor.

Table 3 provides the SI between the above-mentioned hemodynamics descriptors and oxygen polarization, represented by SH10, for RCA and Carotid 2.

	TAWSS10	**OSI90**	**RRT90**	**TransWSS90**	**DIV10**
RCA	0,1901	0,2811	0,3614	0,0014	0,3805
Carotid 2	0,2118	0,2487	0,3792	0	0,4267

Table 3 Similarity index between SH10 and each hemodynamics descriptor.

Lastly, **Table 4** represents the SI between LDL90 and SH10 for RCA and Carotid 2.

	SI
RCA	0,5794
Carotid 2	0,6008

Table 4 Similarity index between LDL90 and SH10 for RCA and Carotid 2.

To better understand the obtained results in terms of co-localization, the Similarity Index was represented by bar graphs, as shown in the figures below.

The co-occurrence of LDL90 with WSS contraction regions is higher than the co-occurrence with the classical descriptors in all cases. As for RCA (**Fig 3.8**), SI has a value almost equal to 0.4 for contraction regions and 0.2 for TAWSS10, OSI90 and RRT90.

The difference is less pronounced for LAD (**Fig. 3.9**) and Carotid 2 (**Fig. 3.11**). In the first case we observe an SI slightly higher than 0.2 (for DIV10) and an SI slightly lower than 0.2 (TAWSS10, OSI90 and RRT90); while for carotid 2 the SI is slightly higher than 0.6 (for DIV10) and slightly lower than 0.6 (for TAWSS10, OSI90 and RRT90). There is a marked difference in the case of Carotid 1, where the SI of the contraction zones is about twice the SI of TAWSS10, OSI90 and RRT90 (**Fig. 3.10**).

For all arterial districts, transWSS has proved not an adequate descriptor for LDL polarization, since it presents a SI equal to 0 (or close to zero) in all cases.

With regard to the similarity analysis between hemodynamic descriptors and oxygen concentration, very similar results were found between RCA (**Fig. 3.12**) and Carotid 2 (**Fig. 3.13**). The SI of the contraction zones is slightly higher than the SI of RRT90. While, OSI90 and TAWSS10 have a SI much lower than DIV10. In particular, there is a decreasing trend of the SI passing from RRT90 to OSI90 and, then, to TAWSS10.

Also in this case, transWSS90 does not co-localize with oxygen concentration polarization (SI=0).

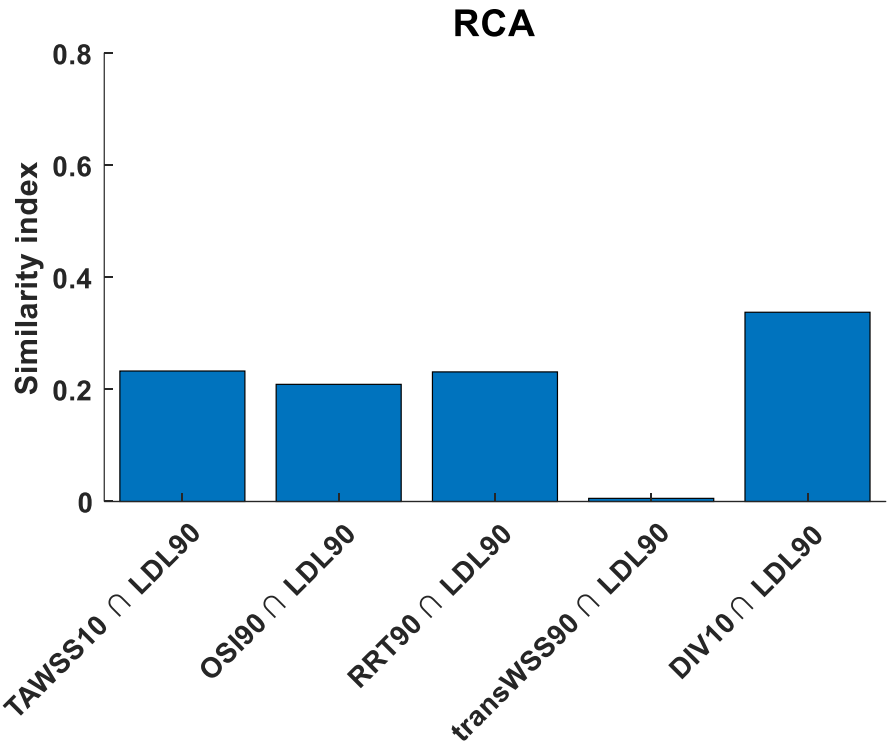

Figure 3.8 Similarity analysis between LDL90 and each hemodynamics descriptor for RCA.

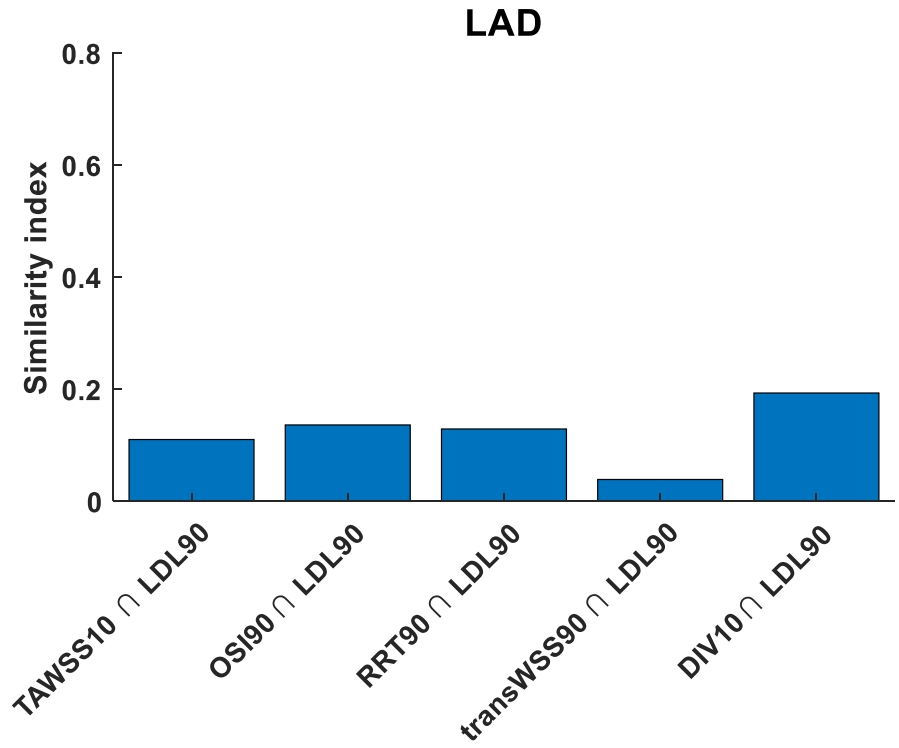

Figure 3.9 Similarity analysis between LDL90 and each hemodynamics descriptor for LAD.

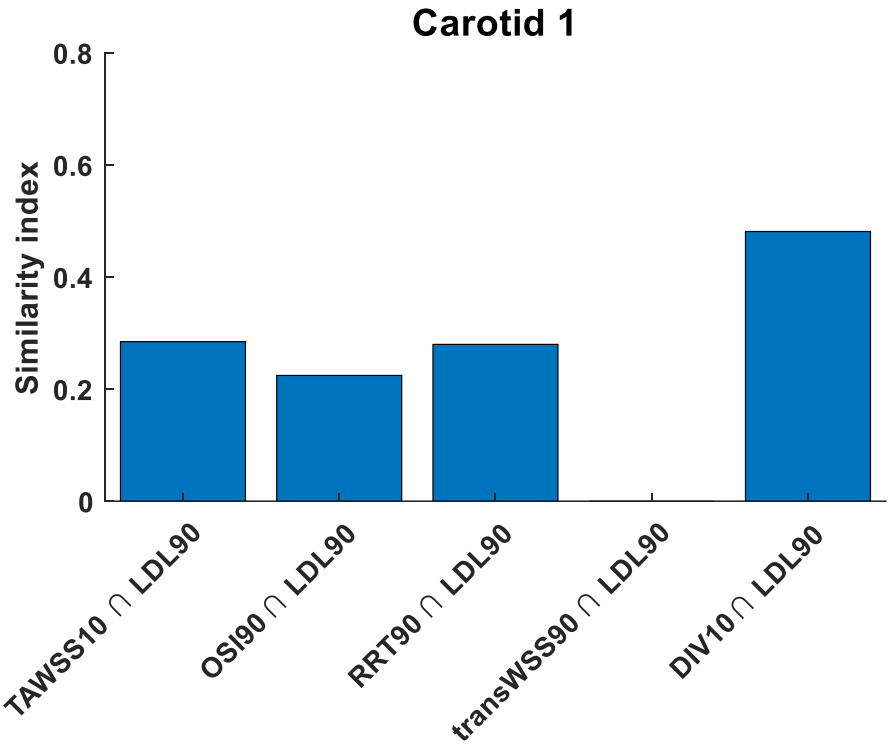

Figure 3.10 Similarity analysis between LDL90 and each hemodynamics descriptor for Carotid 1.

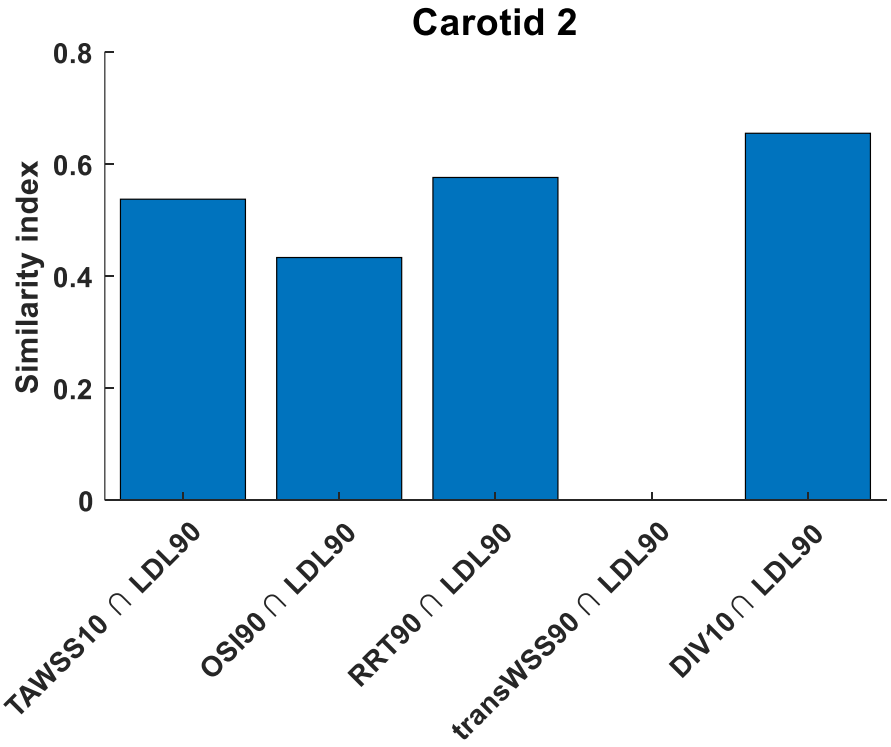

Figure 3.11 Similarity analysis between LDL90 and each hemodynamics descriptor for Carotid 2.

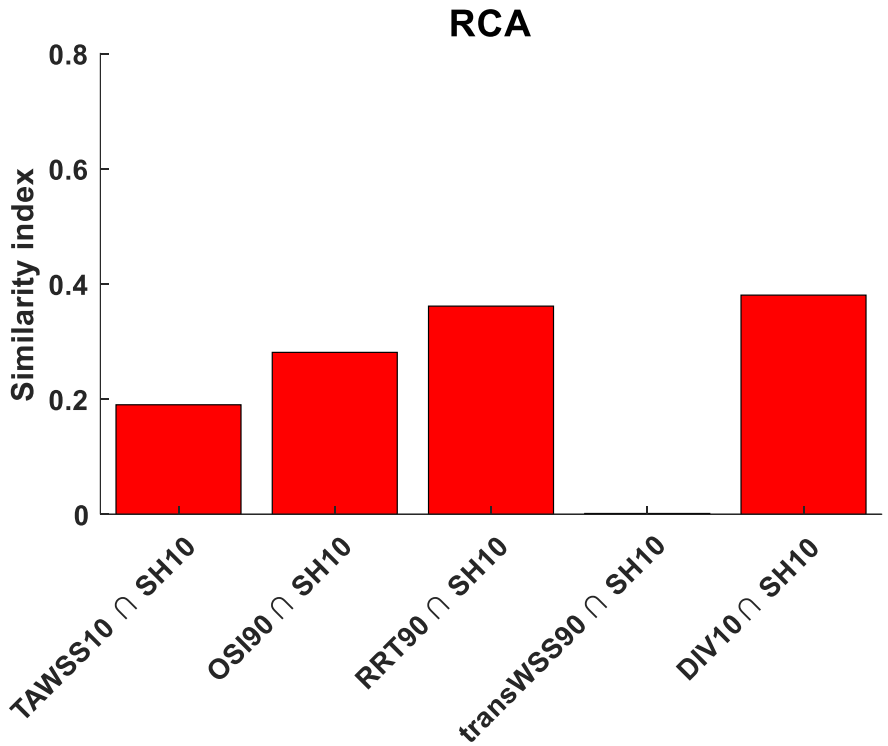

Figure 3.12 Similarity analysis between LDL90 and each hemodynamics descriptor for RCA.

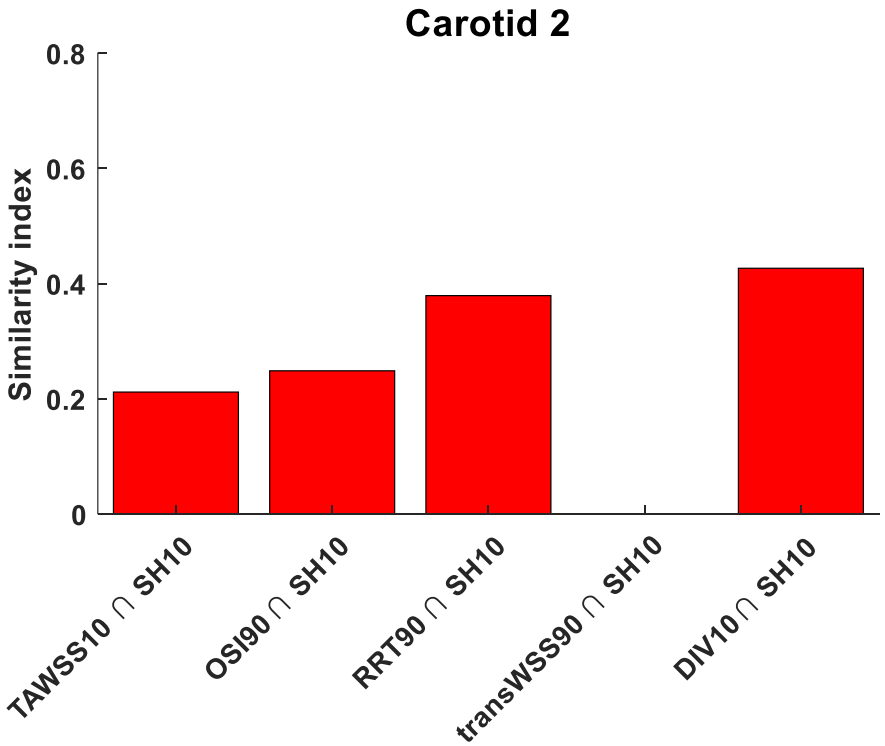

Figure 3.13 Similarity analysis between LDL90 and each hemodynamics descriptor for RCA.

To further appreciate the predominance of the WSS contraction zones as a marker of the LDL and oxygen polarization zones, the percentage difference between the SI of the contraction zones and the SI of respectively TAWSS10, OSI90 and RRT90 was computed. In light of the results previously obtained, in this analysis transWSS90 was neglected.

As regards LDL concentration, the percentage differences between the SI range from a minimum of 15% (for Carotid 2) to a maximum of 100% (for Carotid 1). Carotid 2 (**Fig. 3.17**) is the artery showing the lowest percentage differences of SI between DIV10 and the other hemodynamic descriptors, with a maximum of 50% for OSI90. On the contrary, Carotid 1 (**Fig. 3.16**) is the artery showing the greatest percentage differences between SI, with a maximum of 100% for OSI90. RCA presents the same pattern of Carotid 1 and Carotid 2 in terms of percentage differences but with intermediate values between the two districts (**Fig 3.14**). As for the LAD, the greater percentage difference between SI is for the couple DIV10 - TAWSS10 (75%) (**Fig. 3.15**).

Concerning oxygen concentration, Carotid 2 has the same pattern of percentage differences as RCA: both with a maximum of 100% for TAWSS 10 and a minimum of 5% (RCA) and 15% (Carotid 2) for RRT90 (**Fig. 3.18**, **Fig. 3.19**).

The results show that the performance of the WSS topological skeleton, denoted by DIV10, is in most cases clearly higher than the performance of classical hemodynamic descriptors, thus confirming the reliability of the divergence of normalized WSS as a template of near-wall mass transfer.

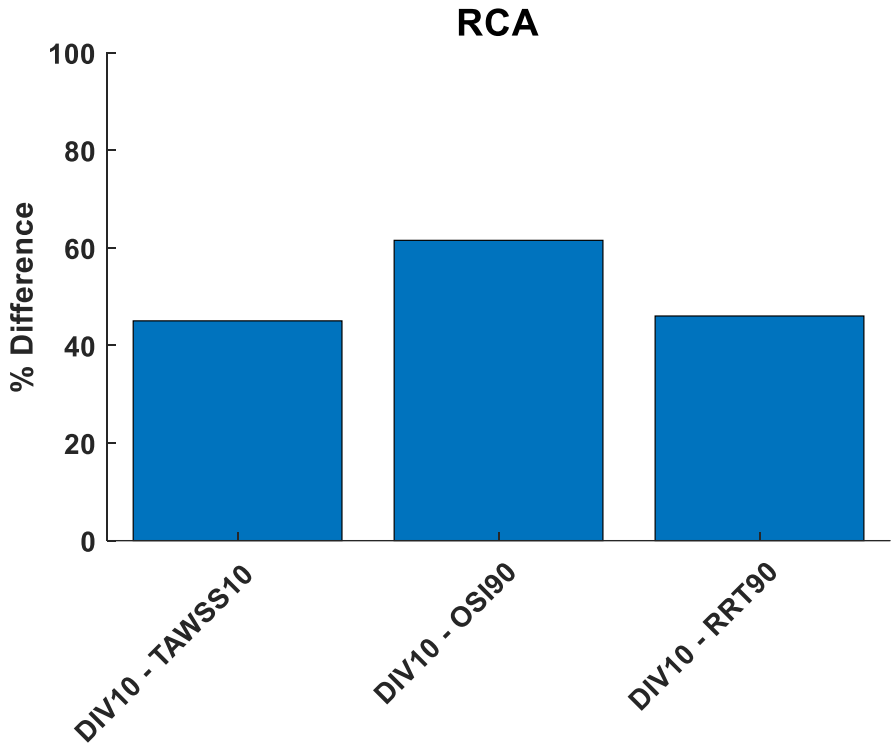

Figure 3.14 Percentage difference between SI of LDL90-DIV10 and respectively SI of LDL90-TAWSS10, LDL90-OSI90, LDL90-RRT90 for RCA.

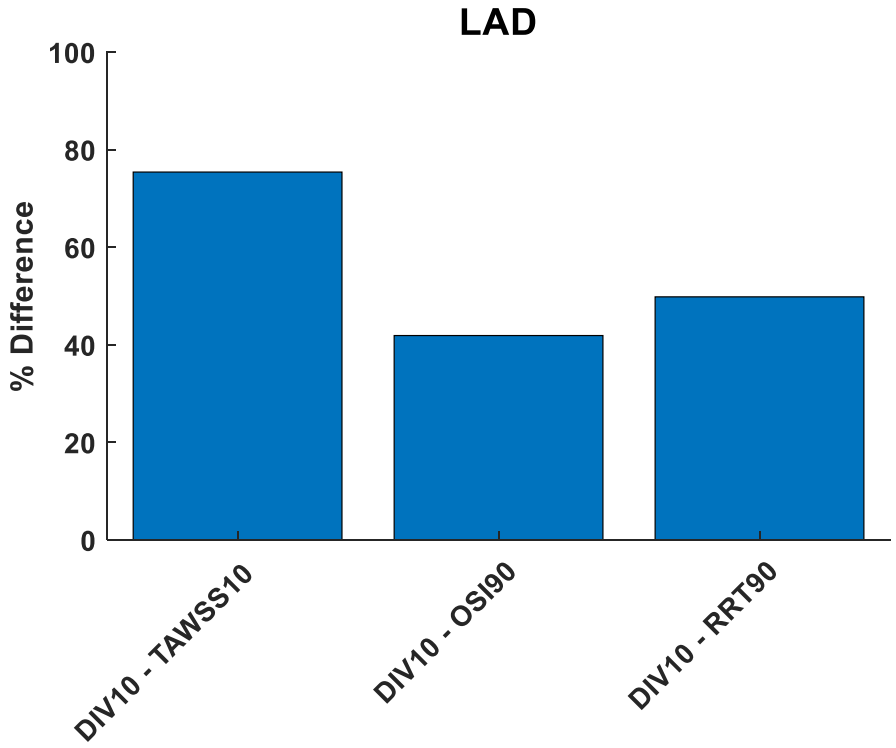

Figure 3.15 Percentage difference between SI of LDL90-DIV10 and respectively SI of LDL90-TAWSS10, LDL90-OSI90, LDL90-RRT90 for LAD.

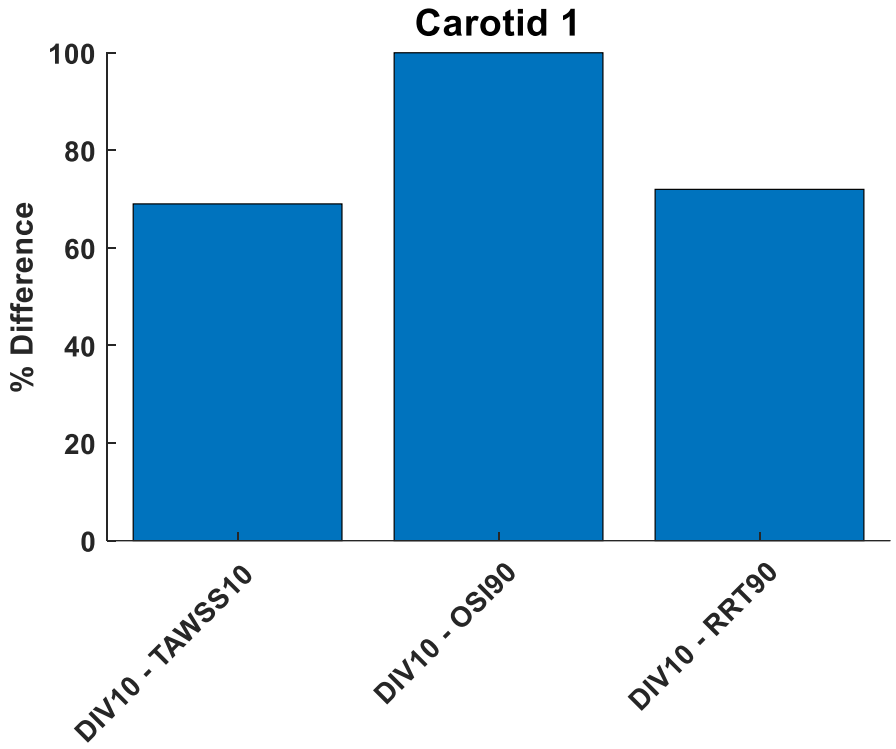

Figure 3.16 Percentage difference between SI of LDL90-DIV10 and respectively SI of LDL90-TAWSS10, LDL90-OSI90, LDL90-RRT90 for Carotid 1.

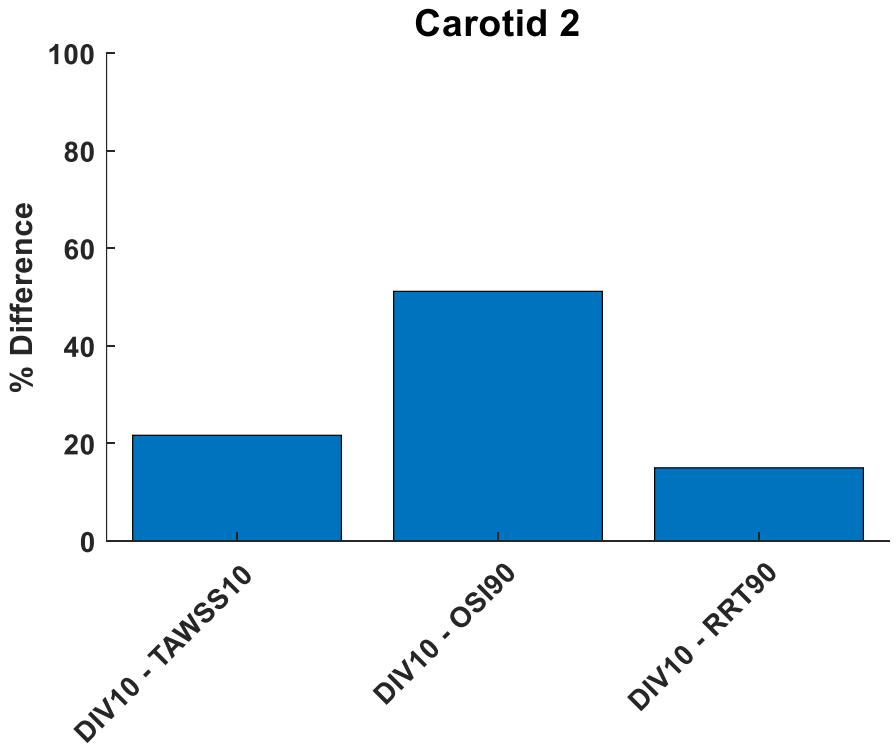

Figure 3.17 Percentage difference between SI of LDL90-DIV10 and respectively SI of LDL90-TAWSS10, LDL90-OSI90, LDL90-RRT90 for Carotid 2.

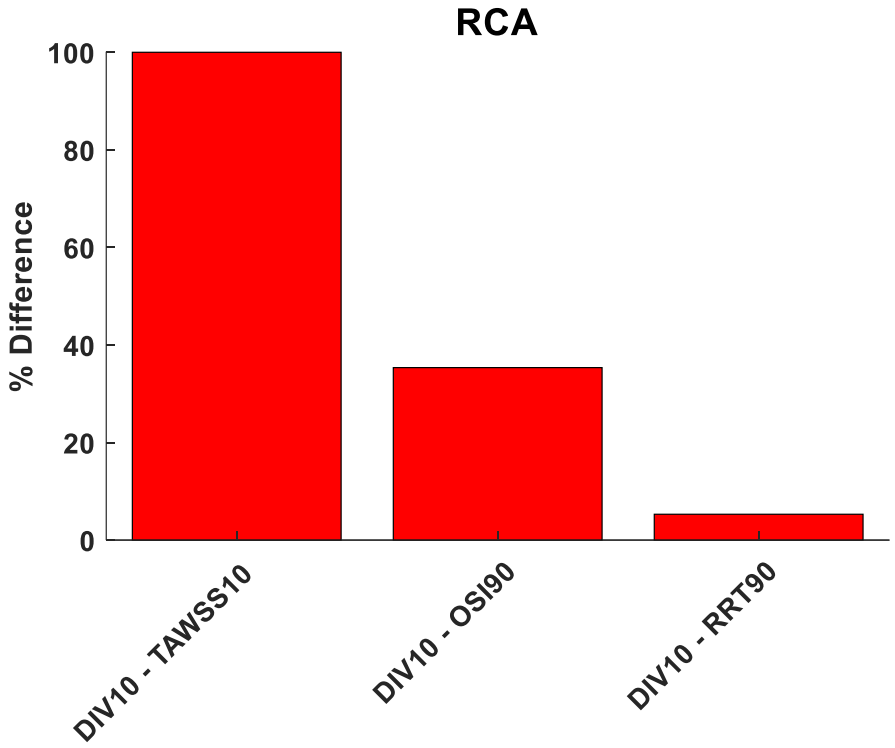

Figure 3.18 Percentage difference between SI of SH10-DIV10 and respectively SI of SH10-TAWSS10, SH10-OSI90, SH10-RRT90 for RCA.

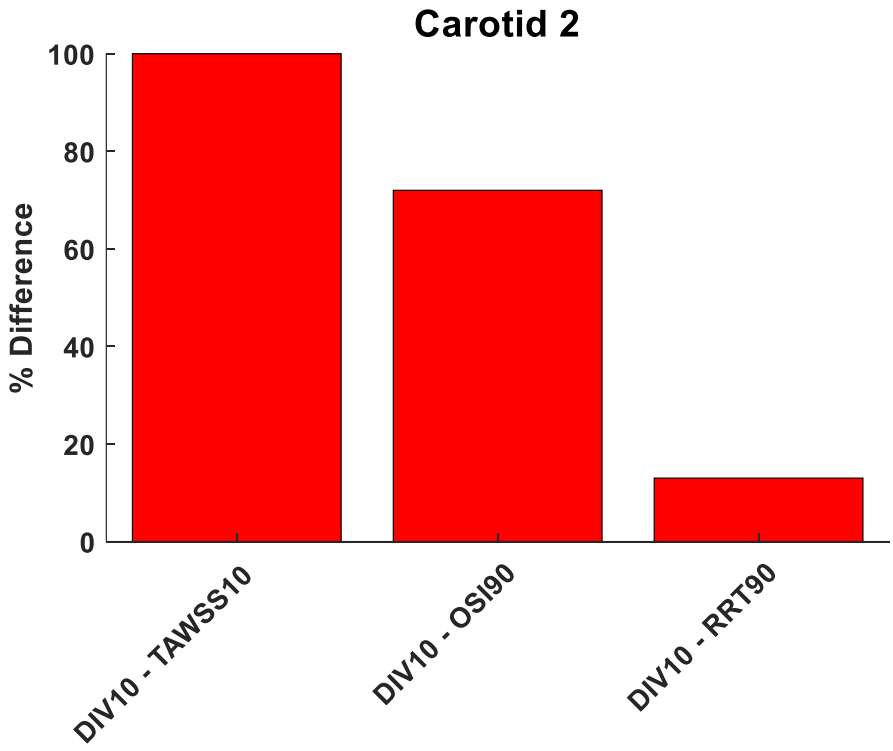

Figure 3.19 Percentage difference between SI of SH10-DIV10 and respectively SI of SH10-TAWSS10, SH10-OSI90, SH10-RRT90 for Carotid 2.

Chapter 4

4 Discussions and conclusions

Atherosclerosis is a complex multifactorial process promoted, among all the other risk factors, by high levels of low-density lipoproteins (LDL) and low levels of oxygen in the arterial wall.

The so-called hemodynamic risk hypothesis, which suggests a key role of altered local hemodynamics in vascular pathophysiology, has led to an increasing interest in the analysis of hemodynamics features in blood vessels. In particular, the fluid forces exerted by the flowing blood on the endothelial cells of the vessel wall are represented by the WSS [56].

Generally, atherosclerotic plaques occur in regions characterized by flow separation and complex secondary and recirculation flows ("disturbed flow"), where WSS is typically low and oscillating [58, 63, 64].

Several hemodynamic descriptors have been proposed over the years in order to evaluate the impact of different pattern of WSS on the vessel wall. Typically, in presence of laminar and unidirectional flow, characterized by high WSS magnitudes, endothelial cells tend to align in the direction of the flow leading to an organized layer. On the contrary, cells subjected to a disturbed flow, with low and multidirectional WSS, assume a polygonal conformation without a clear orientation, thus widening the intercellular junctions and increasing the wall permeability to atherogenic molecules, e.g. LDL [34].

However, recent studies have suggested that hemodynamic descriptors based only upon WSS magnitude and/or direction may oversimplify the complex hemodynamic milieu to which the luminal surface is exposed. In particular, in the context of atherosclerosis, it was demonstrated that the low/oscillatory WSS phenotype is a significant but moderately weak predictor of lesions localization [62] or endothelial dysfunction at the early stage [42]. In this scenario, a growing interest has recently emerged on WSS vector field topological skeleton, thanks to its potential link with vascular cell biology lying in (1) its ability to quantify the complex and highly dynamic WSS features, and (2) its strong link with features like flow stagnation, separation, and recirculation, which are usually classified as "aggravating flow events" and in turn linked

to “aggravating biological events” [35]. Moreover, recent studies have demonstrated the ability of WSS topological skeleton to properly describe near-wall mass transport in human arteries [34], highlighting the link between the cycle-average WSS topological skeleton and the near-wall biochemical transport in arteries of, e.g., LDL or oxygen [56]. Such phenomena are strictly related to the vascular pathophysiology, such as the wall degradation in ascending thoracic aorta aneurism [36] and late restenosis in endarterectomized carotid arteries [37].

Moving from these evidences, a Eulerian method for WSS topological skeleton analysis based on WSS vector field divergence has been recently proposed to overcome the limitations of the classical Lagrangian techniques, in terms of computational costs and methodological complexity [34].

In the present work the Eulerian methodology is applied to compute WSS topological skeleton in four patient-specific computational models of arteries, i.e. two carotid bifurcations, and two coronary artery models [34]. The aim of this analysis is to test the ability of this method in providing an affordable and sufficiently accurate template of near wall mass-transport.

The performance of this method was first evaluated in terms of a co-localization between WSS contraction regions, denoted by DIV10, and the areas with the highest/lowest accumulation of LDL/oxygen (respectively called LDL90 and SH10). The co-localization analysis was performed through the calculation of the similarity index SI, which quantified the spatial overlap between DIV10 and LDL90 (or SH10). Then, the performance of the WSS topological skeleton analysis was compared with that of the classical hemodynamic descriptors of disturbed flow, through the analysis of the SI.

The findings of this study: (1) confirm that WSS manifolds can be used as reliable template of near-wall mass transport in cardiovascular flows [34]; (2) demonstrate that the recently proposed Eulerian-based method to identify WSS topological skeleton provides an effective template of the LDL and oxygen blood-to-wall transfer.

Moreover, WSS contraction regions markedly co-localize with LDL (and oxygen) luminal polarization, better than canonical WSS-based descriptors of flow disturbance (TAWSS, OSI, RRT and transWSS).

In conclusion, the Eulerian methodology for the identification of WSS topological skeleton, requiring less computational efforts with respect to a fully 3D simulations of

mass transport in cardiovascular flows, candidates as a surrogate marker of near-wall mass transfer, avoiding to solve the computationally expensive advection-diffusion equations [61]. Based on the reported evidences about the physiological significance of the WSS topological skeleton in cardiovascular flows, further investigations elucidating its effects on vascular disease are strongly encouraged and warranted [56].

References

[1] G.J. Tortora and B.H. Derrickson. *Principles of Anatomy and Physiology* 14th Edition: 14th Edition". In: Wiley, 2013. ISBN: 9781118808856.

[2] E.N. Marieb, P.B. Wilhelm, and J.B. Mallatt. *Human Anatomy, Global Edition*. In: Pearson Education Limited, 2016. ISBN: 9781292156873.

[3] I. Peate and M. Nair. *Fundamentals of Anatomy and Physiology: For Nursing and Healthcare Students*. In: Fundamentals. Wiley, 2016. ISBN: 9781119055525.

[4] Weinhaus A.J. (2015) *Anatomy of the Human Heart*. In: Iaizzo P. (eds) Handbook of Cardiac Anatomy, Physiology, and Devices. Springer, Cham. URL: https://doi.org/10.1007/978-3-319-19464-6_5

[5] Britannica, The Editors of Encyclopaedia. *Carotid artery*. Encyclopedia Britannica, 14 Oct. 2008, https://www.britannica.com/science/carotid-artery. Accessed 16 May 2021.

[6] Henry Gray (1821–1865), *Anatomy of the Human Body*, 1918.

[7] Scanlon, Valerie C., and Tina Sanders. 2007. *Essentials of Anatomy and Physiology*. 5th ed. Philadelphia, PA: F.A. Davis Company.

[8] [https://www.webmd.com/heart-disease/carotid-artery-disease-causes-symptoms-tests-and-treatment]

[9] Slides from the course *Biomechanics of the cardiovascular system*"- U. Morbiducci

[10] Gimbrone MA, García-Cardeña G. *Vascular endothelium, hemodynamics, and the pathobiology of atherosclerosis*. Cardiovasc Pathol. 2013;22(1):9-15. doi:10.1016/j.carpath.2012.06.006

[11] URL: https://www.mayoclinic.org/diseases-conditions/arteriosclerosis-atherosclerosis/symptoms-causes/syc-20350569

[12] Nucleus Medical Media (2019). *Aterosclerosi* Retrieved from //nmal.nucleusmedicalmedia.com/aterosclerosi/view-item?ItemID=72277.

[13] Badimon JJ, Fuster V, Chesebro JH, Badimon L. *Coronary atherosclerosis. A multifactorial disease*. *Circulation*. 1993 Mar;87(3 Suppl): II3-16. PMID: 8443920.

[14] Llorente-Cortes, V. and Badimon, L., 2005. *LDL receptor-related protein and the vascular wall: implications for atherothrombosis.*

[15] Arterioscler Thromb Vasc Biol 25(3): 497-504.Segrest, J. P., Jones, M. K., De Loof, H. and Dashti, N., 2001. *Structure of apolipoprotein B-100 in low density lipoproteins.* J Lipid Res 42(9): 1346-1367.

[16] Bancells, C., Canals, F., Benitez, S., Colome, N., Julve, J., OrdonezLlanos, J. and Sanchez-Quesada, J. L., 2010. *Proteomic analysis of electronegative low-density lipoprotein.* J Lipid Res 51(12): 3508- 3515.

[17] Badimon, L. and Vilahur, G., 2012. *LDL-cholesterol versus HDL cholesterol in the atherosclerotic plaque: inflammatory resolution versus thrombotic chaos.* Ann N Y Acad Sci 1254: 18-32.

[18] Oörni K, Pentikäinen MO, Ala-Korpela M, Kovanen PT. *Aggregation, fusion, and vesicle formation of modified low density lipoprotein particles:*

molecular mechanisms and effects on matrix interactions. J Lipid Res. 2000 Nov;41(11):1703-14. PMID: 11060340.

[19] Li, D. and Mehta, J. L., 2000. *Antisense to LOX-1 inhibits oxidized LDL-mediated upregulation of monocyte chemoattractant protein-1 and monocyte adhesion to human coronary artery endothelial cells.* Circulation 101(25): 2889-2895.

[20] Sawamura, T., Kume, N., Aoyama, T., Moriwaki, H., Hoshikawa, H., Aiba, Y., Tanaka, T., Miwa, S., Katsura, Y., Kita, T. and Masaki, T., 1997. *An endothelial receptor for oxidized low-density lipoprotein.* Nature 386(6620): 73-77.

[21] Nievelstein, P. F., Fogelman, A. M., Mottino, G. and Frank, J. S., 1991. *Lipid accumulation in rabbit aortic intima 2 hours after bolus infusion of low density lipoprotein. A deep-etch and immunolocalization study of ultrarapidly frozen tissue.* Arterioscler Thromb 11(6): 1795-1805.

[22] Llorente-Cortes, V., Otero-Vinas, M., Hurt-Camejo, E., MartinezGonzalez, J. and Badimon, L., 2002a. *Human coronary smooth muscle cells internalize versican-modified LDL through LDL receptor-related protein and LDL receptors.* Arterioscler Thromb Vasc Biol 22(3): 387- 393.

[23] Buton, X., Mamdouh, Z., Ghosh, R., Du, H., Kuriakose, G., Beatini, N., Grabowski, G. A., Maxfield, F. R. and Tabas, I., 1999. *Unique cellular events occurring during the initial interaction of macrophages with matrix-retained or methylated aggregated low-density lipoprotein (LDL). Prolonged cell-surface contact during which ldl-cholesteryl ester hydrolysis exceeds ldl protein degradation.* J Biol Chem 274(45): 32112-32121.

[24] Tabas, I., Williams, K. J. and Boren, J., 2007. *Subendothelial lipoprotein retention as the initiating process in atherosclerosis: update and therapeutic implications.* Circulation 116(16): 1832-1844.

[25] Segrest, J. P., Jones, M. K., De Loof, H. and Dashti, N., 2001. *Structure of apolipoprotein B-100 in low density lipoproteins.* J Lipid Res 42(9): 1346-1367.

[26] https://www.britannica.com/science/human-respiratory-system/Transport-of-oxygen

[27] Ritman EL, Lerman A. 2007 *The dynamic vasa vasorum*. Cardiovasc. Res. 75, 649–658. (doi:10. 1016/j.cardiores.2007.06.020)

[28] Wolinsky H, Glagov S. 1967 *Nature of species differences in the medial distribution of aortic vasa vasorum in mammals*. Circ. Res. 20, 409–421. (doi:10.1161/01.RES.20.4.409)

[29] Williams JK, Armstrong ML, Heistad DD. 1988 *Vasa vasorum in atherosclerotic coronary arteries: responses to vasoactive stimuli and regression of atherosclerosis.* Circ. Res. 62, 515–523. (doi:10. 1161/01.RES.62.3.515)

[30] Choi BJ, Matsuo Y, Aoki T, Kwon T-G, Prasad A, Gulati R, Lennon RJ, Lerman LO, Lerman A. 2014 *Coronary endothelial dysfunction is associated with inflammation and vasa vasorum proliferation in patients with early atherosclerosis.* Arterioscler. Thromb. Vasc. Biol. 34, 2473–2477. (doi:10.1161/ ATVBAHA.114.304445)

[31] Tarbell J, Mahmoud M, Corti A, Cardoso L, Caro C. 2020 *The role of oxygen transport in atherosclerosis and vascular disease*. J. R. Soc. Interface 17: 20190732. http://dx.doi.org/10.1098/rsif.2019.0732

[32] Semenza GL. 2012 *Hypoxia-inducible factors in physiology and medicine*. Cell 148, 399–408. (doi:10.1016/j.cell.2012.01.021)

[33] Wootton, D.M., Ku, D.N., 1999. *Fluid mechanics of vascular systems, diseases, and thrombosis.* Annual Review of Biomedical Engineering 1, 299-329.

[34] G. De Nisco, V. Mazzi, K. Calò et al. 2020. *Eulerian-based wall shear stress topological skeleton analysis and near-wall transport in aortic flow.* GNB2020

[35] Mazzi V, Gallo D, Calò K, Najafi M, Khan MO, De Nisco G, Steinman DA, Morbiducci U. *A Eulerian method to analyze wall shear stress fixed points and manifolds in cardiovascular flows*. Biomech Model Mechanobiol. 2020 Oct;19(5):1403-1423. doi: 10.1007/s10237-019-01278-3. Epub 2019 Dec 21. PMID: 31865482.

[36] Giuseppe De Nisco, Paola Tasso, Karol Calò, Valentina Mazzi, Diego Gallo, Francesca Condemi, Solmaz Farzaneh, Stéphane Avril, Umberto Morbiducci. *Deciphering ascending thoracic aortic aneurysm hemodynamics in relation to biomechanical properties*. Medical Engineering & Physics,Volume 82, 2020, Pages 119-129, ISSN 1350-4533, https://doi.org/10.1016/j.medengphy.2020.07.003.

[37] Morbiducci, U., Mazzi, V., Domanin, M. *et al. Wall Shear Stress Topological Skeleton Independently Predicts Long-Term Restenosis After Carotid Bifurcation Endarterectomy.* Ann Biomed Eng 48, 2936–2949 (2020). https://doi.org/10.1007/s10439-020-02607-9

[38] Feng S et al. 2017 *Mechanical activation of hypoxiainducible factor 1α drives endothelial dysfunction at atheroprone sites*. Arter. Thromb. Vasc. Biol. 37, 2087–2101. (doi:10.1161/ATVBAHA.117.309249)

[39] Wu D et al. 2017 *HIF-1α is required for disturbed flow-induced metabolic reprogramming in human and porcine vascular endothelium*. eLife 6, e25217. (doi:10.7554/elife.25217.044)

[40] Slides from the course *Biomechanics of the cardiovascular system* - U. Morbiducci "On Uncertainty, Verification, Validation of Cardiovascular CFD Models"

[41] Calò K, Gallo D, Steinman DA, Mazzi V, Scarsoglio S, Ridolfi L, Morbiducci U. *Spatiotemporal Hemodynamic Complexity in Carotid Arteries: An Integrated Computational Hemodynamics and Complex Networks-Based Approach.* IEEE Trans Biomed Eng. 2020 Jul;67(7):1841-1853. doi: 10.1109/TBME.2019.2949148. Epub 2019 Oct 23. PMID: 31647419.

[42] Gallo D. et al. 2018 *Segment-specific associations between local haemodynamic and imaging markers of early atherosclerosis at the carotid artery*: *an in vivo human study*. J. R. Soc. Interface 15: 20180352. http://dx.doi.org/10.1098/rsif.2018.0352

[43] De Nisco G, Kok AM, Chiastra C, Gallo D, Hoogendoorn A, Migliavacca F, Wentzel JJ, Morbiducci U. *The Atheroprotective Nature of Helical Flow in Coronary Arteries.* Ann Biomed Eng. 2019 Feb;47(2):425-438. doi: 10.1007/s10439-018-02169-x. Epub 2018 Nov 28. PMID: 30488307 - Supplementar Material

[44] Steinman DA, Thomas JB, Ladak HM, Milner JS, Rutt BK, Spence JD. *Reconstruction of carotid bifurcation hemodynamics and wall thickness using computational fluid dynamics and MRI*. Magn Reson Med. 2002 Jan;47(1):149-59. doi: 10.1002/mrm.10025. PMID: 11754454.

[45] De Santis G, Mortier P, De Beule M, Segers P, Verdonck P, Verhegghe B. *Patient-specific computational fluid dynamics: structured mesh generation from*

coronary angiography. Med Biol Eng Comput. 2010 Apr;48(4):371-80. doi: 10.1007/s11517-010-0583-4. Epub 2010 Feb 17. PMID: 20162466.

[46] Liu X, Fan Y, Deng X. *Effect of spiral flow on the transport of oxygen in the aorta: a numerical study*. Ann Biomed Eng. 2010 Mar;38(3):917-26. doi: 10.1007/s10439-009-9878-8. Epub 2009 Dec 24. PMID: 20033776.

[47] Liu X, Fan Y, Deng X, Zhan F. *Effect of non-Newtonian and pulsatile blood flow on mass transport in the human aorta*. J Biomech. 2011 Apr 7;44(6):1123-31. doi: 10.1016/j.jbiomech.2011.01.024. PMID: 21310418.

[48] Wada S, Karino T. *Theoretical prediction of low-density lipoproteins concentration at the luminal surface of an artery with a multiple bend*. Ann Biomed Eng. 2002 Jun;30(6):778-91. doi: 10.1114/1.1495868. PMID: 12220078.

[49] Deng X.Y., Marois Y., How T., Merhi Y., King M., Guidoin R., Karino T., *Luminal surface concentration of lipoprotein (LDL) and its effect on the wall uptake of cholesterol by canine carotid arteries.* J Vasc Surg 21: 135–145, 1995.

[50] Lee S. W., Antiga L., Steinman D. A., *Correlations among indicators of disturbed flow at the normal carotid bifurcation.* J Biomech Eng, 2009.

[51] Malek A. M., Alper S. L., Izumo S., *Hemodynamic shear stress and its role in atherosclerosis*. JAMA, 1999

[52] Dolan J. M., Kolega J., Meng H.., *High Wall Shear Stress and Spatial Gradients in Vascular Pathology: A Review*. Ann Biomed Eng., 2013.

[53] Gallo D., Isu G., Massai D., Pennella F., Deriu M. A., Ponzini R., Bignardi C., Audenino A. Rizzo G., Morbiducci U., *A survey of quantitative descriptors of arterial flows*. Biomedical Engineering, 2014.

[54] Arzani, A., Gambaruto, A.M., Chen, G. et al. *Wall shear stress exposure time: a Lagrangian measure of near-wall stagnation and concentration in cardiovascular flows.* Biomech Model Mechanobiol 16, 787–803 (2017). https://doi.org/10.1007/s10237-016-0853-7

[55] Tada S. *Numerical study of oxygen transport in a carotid bifurcation*. Phys Med Biol. 2010 Jul 21;55(14):3993-4010. doi: 10.1088/0031-9155/55/14/004. Epub 2010 Jun 24. PMID: 20577040.

[56] Mazzi, V.; Morbiducci, U.; Calò, K.; De Nisco, G.; Lodi Rizzini, M.; Torta, E.; Caridi, G.C.A.; Chiastra, C.; Gallo, D. *Wall Shear Stress Topological Skeleton Analysis in Cardiovascular Flows: Methods and Applications.* Mathematics 2021, *9*, 720. https://doi.org/10.3390/math9070720.

[57] Moore JA, Ethier CR. *Oxygen mass transfer calculations in large arteries*. J Biomech Eng. 1997 Nov;119(4):469-75. doi: 10.1115/1.2798295. PMID: 9407287.

[58] Ku DN, Giddens DP, Zarins CK, Glagov S. Pulsatile flow and atherosclerosis in the human carotid bifurcation. Positive correlation between plaque location and low oscillating shear stress. Arteriosclerosis. 1985 May-Jun; 5(3):293-302. doi: 10.1161/01.atv.5.3.293. PMID: 3994585.

[59] Himburg HA, Grzybowski DM, Hazel AL, LaMack JA, Li XM, Friedman MH. *Spatial comparison between wall shear stress measures and porcine arterial endothelial permeability.* Am J Physiol Heart Circ Physiol. 2004 May;286(5):H1916-22. doi: 10.1152/ajpheart.00897.2003. Epub 2004 Jan 8. PMID: 14715506.

[60] Peiffer V, Sherwin SJ, Weinberg PD. *Computation in the rabbit aorta of a new metric - the transverse wall shear stress - to quantify the multidirectional character of disturbed blood flow.* J Biomech. 2013 Oct 18;46(15):2651-8. doi:

10.1016/j.jbiomech.2013.08.003. Epub 2013 Aug 30. PMID: 24044966; PMCID: PMC3807647.

[61] De Nisco G., Mazzi V., Calò K. et al. *Exploring the link between wall shear stress topological skeleton and near-wall mass transport in cardiovascular flows using a Eulerian-based method.* SB^{3}C2021, June 14-18.

[62] Peiffer V, Sherwin SJ, Weinberg PD. *Does low and oscillatory wall shear stress correlate spatially with early atherosclerosis?* A systematic review. Cardiovasc Res. 2013 Jul 15;99(2):242-50. doi: 10.1093/cvr/cvt044. Epub 2013 Mar 3. PMID: 23459102; PMCID: PMC3695746.

[63] Caro, C. G., J. M. Fitz-Gerald, and R. C. Schroter. *Arterial wall shear and distribution of early atheroma in man*. Nature (London) 223:1159–1161, 1969.

[64] Friedman, M.H., 1983. *Geometric risk factors for arteriosclerosis*. Johns Hopkins APL Technical Digest (Appl. Phys. Lab.) 4, 85–95.

Figures References

Figure 1.1 Pulmonary and systemic circulation. Available at: https://vcodemy.com//home/blog_view/4.

Figure 1.2 Anterior view of the heart. Available at: https://www.kenhub.com/en/library/learning-strategies/diagrams-quizzes-worksheets-of-the-heart.

Figure 1.3 Carotid arteries: the left side shows the lateral view with a focus of the carotid sinus (green) and the carotid body (yellow) while on the right there is a frontal view. Available at: https://www.kenhub.com/en/study/main-arteries-found-in-neck-and-head.

Figure 1.4 Two different views of the heart with the detail of the coronary arteries (blue vessels). Available at: https://www.kenhub.com/en/study/sternocostal-surface-of-the-heart

Figure 1.5 Structure of a lipoprotein. Available at: https://schoolbag.info/chemistry/mcat_biochemistry/70.html

Figure 1.6 Aggregation and fusion of LDL: native LDL (left), aggregated LDL (middle) and fused LDL (right). Source: https://doi.org/10.1016/S0022-2275(20)31964-7.

Figure 1.7 Structure of hemoglobin. Available at: Britannica, The Editors of Encyclopaedia. "Hemoglobin". Encyclopedia Britannica, 15 Dec. 2020, https://www.britannica.com/science/hemoglobin. Accessed 24 June 2021.

Figure 1.8 Schematic of normoxing and hypoxic signaling. Source: Tarbell John, Mahmoud Marwa, Corti Andrea, Cardoso Luis and Caro Colin 2020The role of oxygen

transport in atherosclerosis and vascular diseaseJ. R. Soc. Interface.172019073220190732 - http://doi.org/10.1098/rsif.2019.0732.

Figure 1.9 Modifications of the endothelial cells in response of laminar unidirectional flow (left) and oscillatory slow flow (right). Source: Malek A. M., Alper S. L., Izumo S., Hemodynamic shear stress and its role in atherosclerosis. JAMA, 1999.

Figure 2.1 Scheme of the coronary arteries geometry reconstruction from medical images. Source: De Nisco G, Kok AM, Chiastra C, Gallo D, Hoogendoorn A, Migliavacca F, Wentzel JJ, Morbiducci U. The Atheroprotective Nature of Helical Flow in Coronary Arteries. Ann Biomed Eng. 2019 Feb;47(2):425-438. doi: 10.1007/s10439-018-02169-x. Epub 2018 Nov 28. PMID: 30488307.

Figure 2.6 Classification of fixed points in a vector field. .A Eulerian method to analyze wall shear stress fixed points and manifolds in cardiovascular flows. Biomech Model Mechanobiol. 2020 Oct;19(5):1403-1423. doi: 10.1007/s10237-019-01278-3. Epub 2019 Dec 21. PMID: 31865482.